

A top-down slow breathing circuit that alleviates negative affect in mice

Received: 7 October 2023

Accepted: 23 September 2024

Published online: 19 November 2024

 Check for updates

Jinho Jhang¹, Sehyung Park^①, Shijia Liu^{1,2,6}, David D. O'Keefe³ & Sung Han^{①,2,4,5} 

Although breathing is primarily automatic, its modulation by behavior and emotions suggests cortical inputs to brainstem respiratory networks, which hitherto have received little characterization. Here we identify in mice a top-down breathing pathway from dorsal anterior cingulate cortex (dACC) neurons to pontine reticular nucleus GABAergic inhibitory neurons (PnC^{GABA}), which then project to the ventrolateral medulla (VLM). dACC→PnC activity correlates with slow breathing cycles and volitional orofacial behaviors and is influenced by anxiogenic conditions. Optogenetic stimulation of the dACC→PnC^{GABA}→VLM circuit simultaneously slows breathing and suppresses anxiety-like behaviors, whereas optogenetic inhibition increases both breathing rate and anxiety-like behaviors. These findings suggest that the dACC→PnC^{GABA}→VLM circuit has a crucial role in coordinating slow breathing and reducing negative affect. Our study elucidates a circuit basis for top-down control of breathing, which can influence emotional states.

Activity within the medulla oblongata controls breathing and responds to chemosensory inputs related to blood gas and pH levels, as well as mechanosensory signals from stretch receptors in the airway and lungs^{1–3}. This automatic process generally continues under unconscious conditions, including sleep, anesthetized and vegetative states^{4,5}. Interestingly, however, breathing can also be voluntarily controlled. Volitional behaviors can alter or compromise (if temporary) breathing rhythms^{6–11}, suggesting top-down neural mechanisms that modulate brainstem breathing networks⁷.

Breathing is also tightly coupled with emotional states. Breathing rates correlate with anticipatory anxiety¹², and hyperventilation or heightened breathing rates are prevailing symptoms of anxiety and panic disorders in humans^{12–15}. Faster breathing rates are also observed in other animals, including laboratory rats and mice, in response to environmental and sensory stressors^{16–18}. By contrast, slow breathing or mindfulness skills are practiced across various cultures to regulate emotions^{19–21}. Thus, while breathing is primarily an automatic process,

it may be modulated by behavioral, voluntary and emotional inputs from suprapontine structures^{2,6,22}, including the cerebral cortex^{7,11,23}. However, precise neural circuits for top-down coordination of breathing and those capable of slowing breathing rates during stressful conditions to relieve negative affect remain unidentified.

Coordination between breathing and voluntary behaviors indicates that brain regions mediating planned behaviors, including the frontal and motor cortices, may also exert control over autonomous breathing circuits^{11,22,24}. Neuroimaging and intracranial recording studies have identified cortical regions in the human brain, such as the anterior cingulate cortex (ACC) and the premotor cortex, which are active during self-aware and voluntary breathing^{22,25} as well as during respiratory challenges^{26–29}. Cortical activation is also observed during oropharyngeal behaviors that require coordination with breathing cycles^{9–11,30,31}, such as swallowing, coughing and vocalization. In rodents, the prefrontal cortex exhibits prominent synchronicity between neuronal oscillations and breathing rhythms^{32,33}.

¹Peptide Biology Laboratory, The Salk Institute for Biological Studies, La Jolla, CA, USA. ²Department of Neurobiology, Division of Biological Sciences, University of California San Diego, La Jolla, CA, USA. ³Research Development Department, The Salk Institute for Biological Studies, La Jolla, CA, USA. ⁴Center for Neuroscience Imaging Research, Institute for Basic Science, Suwon, Republic of Korea. ⁵Department of Biomedical Engineering, Sungkyunkwan University, Suwon, Republic of Korea. ⁶Present address: Howard Hughes Medical Institute, Department of Neurobiology, Harvard Medical School, Boston, MA, USA.  e-mail: sunghan@salk.edu

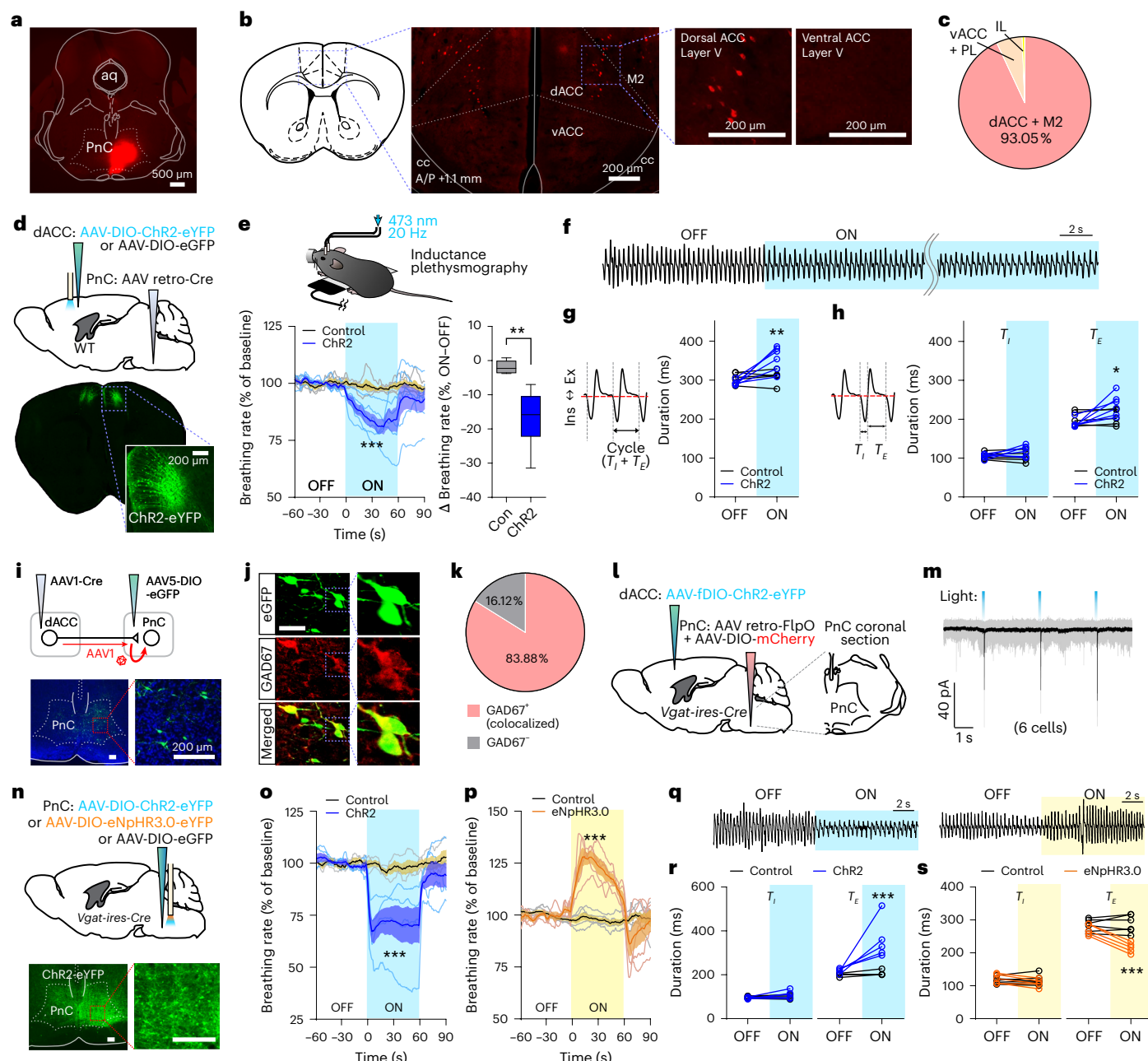


Fig. 1 | Identification of a cortical-to-brainstem slow breathing circuit.

a, Injection of the CTB-555 tracer into the PnC. Scale bar, 500 μm. **b**, CTB-labeled neurons observed in the dACC and M2. Scale bar, 200 μm. **c**, Quantification of CTB-labeled neurons in prefrontal subregions. **d**, Projection-specific expression of AAV constructs in dACC → PnC neurons. Top: schematic representation showing the viral injection. Bottom: the expression of ChR2-eYFP in dACC → PnC neurons. Scale bar, 200 μm. **e**, Inductance plethysmography experiment with photostimulation under anesthesia. Photoactivation of dACC → PnC neurons slows breathing rate. Bottom right: light-induced change (ON-OFF) of breathing rates (percentage of baseline). **f**, Representative raw breathing trace observed during the photoactivation of dACC → PnC neurons in a ChR2-expressing mouse. Scale bar, 2 s. **g,h**, Breathing cycle duration (g) and inspiratory and expiratory phase durations (h) during photoactivation of dACC → PnC neurons (e-h). ChR2, n = 6; eGFP, n = 5 mice. **i**, Anterograde tracing experiment using AAV1-Cre. Bottom: PnC neurons labeled with Cre-dependent expression DIO-eGFP.

Scale bar, 200 μm. **j**, Colocalization between eGFP-labeled neurons and GAD67-immunolabeled signals. **k**, Quantification of colocalized neurons (203 of 242 neurons; n = 5 mice). **l**, Viral injection schematic for slice electrophysiology experiments. **m**, Light-evoked inward currents in PnC^{GABA} neurons. Black trace is an average of all individual traces (gray, n = 6 of 10 cells tested; n = 3 mice). **n**, Cre-dependent AAV expression schematic in PnC^{GABA} neurons. **o**, Photoactivation of PnC^{GABA} neurons slows breathing rate. **p**, Photoinhibition of PnC^{GABA} neurons increases breathing rate. **q**, Representative raw breathing traces observed during photoactivation (left) and photoinhibition (right) of PnC^{GABA} neurons. Scale bar, 2 s. **r,s**, Quantification of inspiratory and expiratory phase durations during photoactivation and photoinhibition of PnC^{GABA} neurons (o,r, ChR2, n = 5; eGFP, n = 4; p,s, eNpHR3.0, n = 5; eGFP, n = 6). *P < 0.05, **P < 0.01 and ***P < 0.001. Line graphs are shown as mean ± s.e.m. or individual values. Box-whisker plot is shown as median and interquartile range with minimum and maximum. PL, prelimbic cortex; aq, aqueduct; IL, infralimbic cortex; WT, wild type.

Pharmacological inhibition of prefrontal subregions (prelimbic and infralimbic areas) abolishes stress-induced breathing responses in rats^{16,17}. Yet, a detailed understanding of respiratory control at the cellular and circuit level is vastly focused on brainstem breathing networks. In this study, we aimed to identify a precise neural circuit responsible for cortical modulation of breathing. We report a subset of neurons in the dorsal ACC (dACC) that project to inhibitory neurons in the pontine reticular nucleus caudalis (PnC) that function to slow down breathing and coordinate breathing with behaviors and emotional states.

Results

Identification of a top-down slow breathing circuit

Previous studies explored inhibitory neurotransmission in medullary breathing circuits, focusing on GABAergic and glycinergic neurons within the pre-Bötzinger complex^{34–37}. In contrast, the function of cortical structures in relaying inhibitory inputs to the ventrolateral medulla (VLM) has been less studied, leaving their functions largely uncharacterized. To identify circuits potentially relaying top-down inhibitory inputs to breathing centers in the brainstem, we performed an extensive search of the Mouse Brain Connectivity Atlas (Allen Brain Institute, <https://connectivity.brain-map.org>) and the *in situ* hybridization (ISH) Atlas (Extended Data Fig. 1a–d). We looked for regions that (1) receive inputs from the prefrontal cortex, (2) project to the VLM and (3) are enriched for markers of inhibitory cell types. A region that satisfied these three criteria (Extended Data Fig. 1a–d) was the PnC. Consistently, a previous tracing study using G-deleted pseudorabies virus as a retrograde tracer reported labeling of the PnC region from somatostatin-positive neurons in the pre-Bötzinger complex³⁸.

To characterize prefrontal neurons that project to the PnC, we performed retrograde tracing using cholera-toxin subunit B (CTB). CTB conjugated with Alexa Fluor 555 was injected into the PnC (Fig. 1a and Supplementary Fig. 1a), revealing CTB-labeled neurons in prefrontal regions (Fig. 1b). Most labeled prefrontal cells (93.05%; 1,219 of 1,310 cells, $n = 5$ mice) were in layer V of the dACC and the secondary motor cortex (M2; Fig. 1c). Only 6.34% and 0.61% were found in other prefrontal subregions—ventral ACC (vACC; with prelimbic cortex) and infralimbic cortex, respectively. Hereafter, we refer to these neurons as dACC→PnC neurons.

To investigate the role of dACC→PnC neurons in controlling breathing, we unilaterally injected the PnC of wild-type mice with a retrograde adeno-associated viral vector encoding Cre recombinase (AAVretro-Cre) and bilaterally injected the dACC with an AAV vector carrying double-floxed inverse open reading frame (DIO) channelrhodopsin-2 (ChR2) fused with enhanced yellow fluorescent protein (AAV-DIO-ChR2-eYFP) or DIO enhanced green fluorescent protein (AAV-DIO-eGFP; Fig. 1d and Supplementary Fig. 1c), resulting in the expression of eGFP or ChR2-eYFP in the dACC (Fig. 1d). Consistent with our tracing results (Fig. 1b,c), only layer V neurons in the dACC/M2 regions were labeled with eYFP. We measured breathing using inductance plethysmography (Fig. 1e) on anesthetized mice fixed in a stereotaxic frame, where a piezoelectric sensor monitors thoracic expansion and contraction. The baseline breathing rate under light anesthesia was maintained at ~200 breaths per minute (BPM), where

the duration of each breath cycle was ~300 ms. Notably, photoactivation of dACC→PnC neurons (20 Hz, 9 mW and 5 ms pulse) significantly reduced breathing rate in the ChR2 group (Fig. 1e and Extended Data Fig. 2a) and accordingly increased the duration of breathing cycles (Fig. 1f,g). No change in breathing rate or cycle duration was observed in controls. We analyzed the contribution of inspiration and expiration to the overall increase in cycle duration. There was no difference in inspiratory duration (T_i) in either ChR2 or control groups, whereas a significant increase in the expiratory duration (T_e) was observed in the ChR2 group (Fig. 1h). The same mice were also tested with reduced light intensities (~6 and ~3 mW; Extended Data Fig. 2b–g). The slowing of breathing rate and increase in T_e were proportional to the intensity of photostimulation (Extended Data Fig. 2d,f). No proportional correlation was observed between T_e and light intensity (Extended Data Fig. 2e). We did not observe apnea interleaved in breathing cycles. These results show that activation of dACC→PnC neurons slows breathing by extending exhalation.

Based on our ISH Atlas search, we predicted that dACC neurons target inhibitory neurons in the PnC (Extended Data Fig. 1c). We tested this by performing anterograde tracing using serotype 1-packaged AAV (AAV1), which *trans*-synaptically travels to efferent neurons^{39,40}. An AAV1 vector encoding Cre recombinase (AAV1-Cre) was injected into the dACC (Fig. 1i), and AAV-DIO-eGFP was injected into the PnC, leading to eGFP expression in the PnC (Fig. 1i, bottom). Because AAV1 may also label neurons in a retrograde manner, we ruled out potential reciprocal connections between the PnC and dACC by injecting CTB-555 tracer into the dACC (Extended Data Fig. 3 and Supplementary Fig. 1b). We did not see PnC neuronal labeling (Extended Data Fig. 3), suggesting that the previous labeling of PnC neurons with the AAV1-Cre tracer likely indicates anterograde delivery from the dACC. Immunostaining of coronal PnC sections with antibodies against glutamic acid decarboxylase 67 (GAD67), a marker of GABAergic cells, showed that 83.88% of neurons (203 of 242 cells, $n = 5$ mice) were colabeled with eGFP and GAD67 (Fig. 1j,k), indicating that dACC neurons project to inhibitory neurons in the PnC. We further validated the dACC→PnC projection through channelrhodopsin-assisted circuit mapping (CRACM) *ex vivo* (Fig. 1l,m). *Vgat-ires-Cre* mice were injected with AAV-DIO-mCherry and AAVretro-FlpO in the PnC, while AAV-fDIO-ChR2 was injected in the dACC. Inward currents in response to light pulses (5 ms and 3 mW) were seen in mCherry-positive cells in the PnC, voltage clamped at -70 mV, indicating that dACC neurons send excitatory projections to PnC VGAT neurons (Fig. 1m). Latency of the optogenetically induced inward currents was 2.28 ± 0.25 ms (mean \pm s.e.m.).

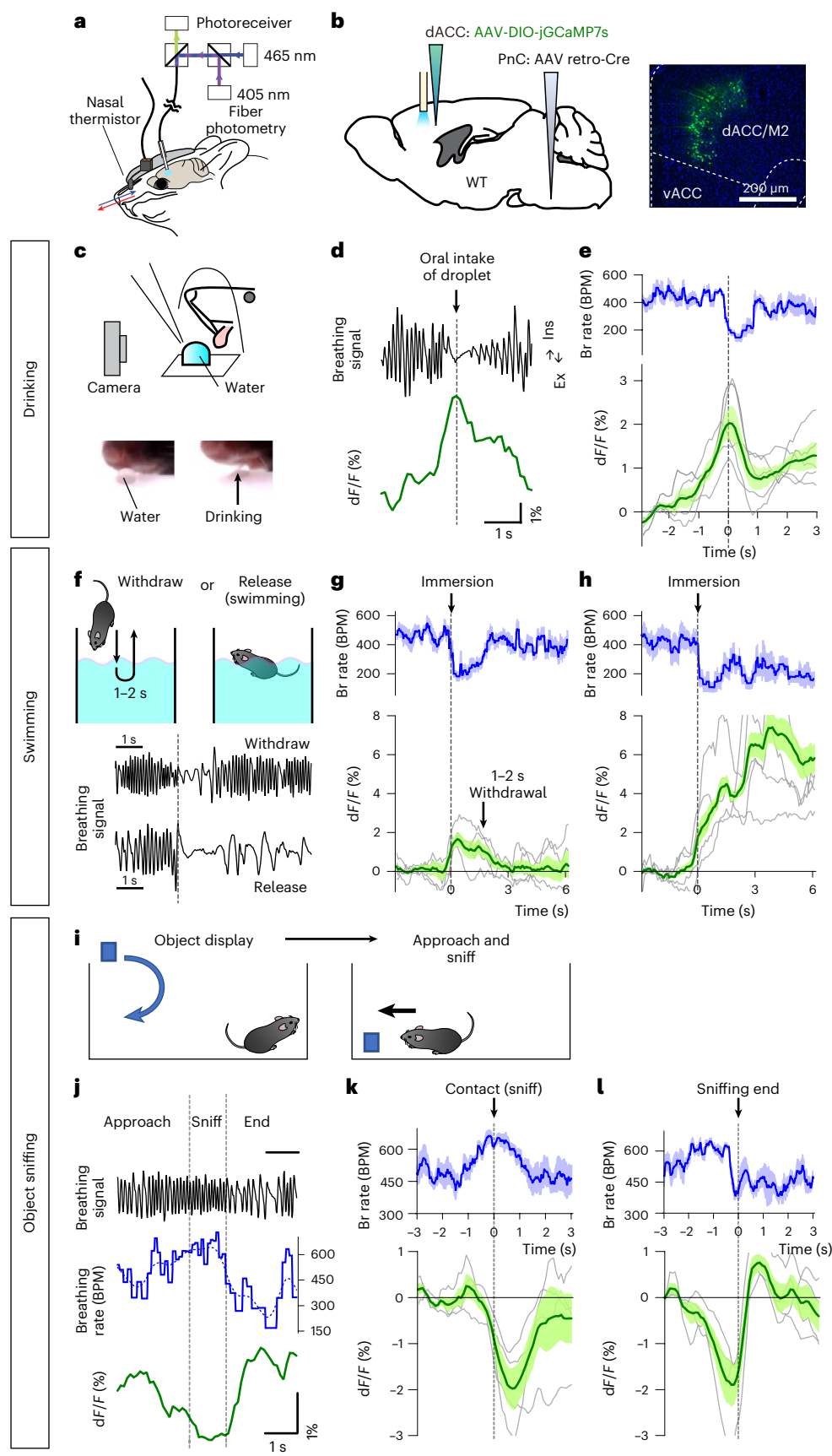
Given these results, we next tested the role of GABAergic PnC neurons (PnC^{GABA}) in controlling breathing using optogenetics. We unilaterally injected AAV-DIO-ChR2-eYFP, AAV-DIO-eNpHR3.0 (halorhodopsin-3.0, an optogenetic inhibitor) or AAV-DIO-eGFP into the PnC of *Vgat-ires-Cre* mice (Fig. 1n and Supplementary Fig. 1d,e). We chose to perform these experiments unilaterally to minimize potentially unwanted behavioral effects due to damage to pontine structures. Mice were anesthetized and monitored using inductance plethysmography. Baseline breathing rates were maintained at ~200 and ~150 BPM for activation and inhibition experiments, respectively.

Fig. 2 | dACC→PnC activities correlate with behaviors that alter breathing. **a**, Simultaneous monitoring of breathing cycles and neuronal calcium activity. **b**, Surgical procedure for expressing jGCaMP7s in dACC→PnC neurons, and image showing jGCaMP7s expression (right). Scale bar, 200 μ m. **c**, Schematic representation showing the observation of voluntary drinking behavior. **d**, Representative traces showing breathing cycles and dACC→PnC activity during drinking behavior. **e**, Average breathing rates (top) and dACC→PnC activity (bottom) during drinking behavior ($n = 5$ mice). Dashed line shows the moment that a water droplet was taken into the oral cavity. **f**, Schematic representation of submersion experiments with two conditions (top) and representative raw breathing traces during withdrawal and submersion tests

(bottom). Scale bar, 1 s. **g,h**, Average breathing rate (top) and dACC→PnC activity (bottom) during withdrawal (g) and release (h) submersion tests ($n = 5$ mice). Dashed lines show the moment that the lower jaw contacts the surface of water. **i**, Schematic representation showing observation of object sniffing behavior. **j**, Representative traces showing raw breathing traces (top), breathing rate (middle) and dACC→PnC neuronal response (bottom). **k**, At the onset of contact-sniffing events, breathing rate increased (above ~600 BPM; top) and dACC→PnC activity decreased (bottom; $n = 4$ mice). **l**, At the end of sniffing events, decreases in breathing rate (top) and rebound-like increases in dACC→PnC activity were observed. Data are shown as mean \pm s.e.m. Gray lines (e,g,h,k,l) show individual traces from each animal.

Photostimulation dramatically decreased breathing rate in the ChR2 group (Fig. 1o,q and Extended Data Fig. 4a), whereas no change was seen in the control group. Conversely, photoinhibition of PnC^{GABA}

neurons increased breathing rate (Fig. 1p,q and Extended Data Fig. 4b). Consistent with the slowed breathing rate, T_E increased during photoactivation of PnC^{GABA} neurons (Fig. 1r), while photoinhibition decreased



T_E (Fig. 1s), but no difference in T_I was seen in any condition (Fig. 1r,s). We did not observe apnea interleaved in breathing cycles during photostimulation.

Previous studies reported that activation or inhibition of the PnC area can modulate fictive masticatory behavior in rabbits⁴¹. We simultaneously video-recorded the jaws of mice during the photoactivation of PnC^{GABA} neurons. However, no instance of mastication or jaw opening was observed, despite dramatic changes in breathing rate (Extended Data Fig. 4c,d).

We next investigated the role of dACC→PnC neurons in controlling breathing in freely moving mice. We implanted a micro-thermistor sensor into the nasal cavity^{5,18,32,42,43} (Extended Data Fig. 2h), which converts the temperature of inspiratory and expiratory cycles into voltage signals. This method enables monitoring of breathing signals without constraining mouse movement. Thermistor-implanted mice were made to express ChR2-eYFP or eGFP in dACC→PnC neurons (same as in Fig. 1d). Mice placed on an elevated platform had a baseline breathing rate of 500 BPM. This breathing rate was stably sustained during the testing session in controls (Extended Data Fig. 2i), whereas the ChR2 group exhibited a significant decrease in breathing rate during photoactivation (Extended Data Fig. 2j).

Our data indicate that both dACC→PnC and PnC^{GABA} neurons can slow breathing rates.

Response of dACC→PnC neurons during volitional behaviors

Because breathing is coordinated with various behaviors that require orofacial and pharyngeal activity^{2,3,8}, we investigated whether the dACC→PnC circuit would be required for this coordination.

We monitored the activity of dACC→PnC and PnC^{GABA} neurons during drinking, a behavior that involves both brainstem and cortical modulation^{10,11,44} and requires apnea (which is distinct from slow breathing). Nevertheless, to explore if PnC^{GABA} neurons may have a role in such volitional behavior, wild-type mice were unilaterally injected with AAVretro-Cre in the PnC, unilaterally injected with AAV-FLEX-jGCaMP7s in the dACC, implanted with an optic fiber over the dACC and implanted with a nasal thermistor sensor (Fig. 2a,b Supplementary Fig. 2a). We monitored breathing and neuronal responses in mice as they voluntarily drank water (Fig. 2c). dACC→PnC neurons were transiently activated at the moment a bolus of water was taken into the mouth cavity (oral phase; Fig. 2d,e). Downstream PnC^{GABA} neuronal activity was monitored in *Vgat-ires-Cre* mice injected with AAV-FLEX-jGCaMP7s in the PnC (Supplementary Fig. 2b and Extended Data Fig. 5a). PnC^{GABA} neural activity recapitulated dACC→PnC neural activity during drinking events (Extended Data Fig. 5b–d). These results demonstrate the activation of both dACC→PnC and PnC^{GABA} neurons during voluntary drinking behavior in mice.

We next monitored dACC→PnC or PnC^{GABA} neural responses during swimming and sniffing. We performed two types of swimming tests that varied with the length of submersion (Fig. 2f). Mice were briefly submerged in water (1–2 s) and then either immediately removed from the water (withdrawal test) or released and allowed to swim (release/swim test). Both conditions induced delayed breaths after the onset of submersion, but with distinct durations (Fig. 2f). During the withdrawal test, alterations in breathing were observed for a short period (~2 s), which then ceased after withdrawal. In contrast, mice displayed repetitions of slowed/delayed breaths during the release/swim test. Notably, increases in dACC→PnC and PnC^{GABA} neuronal responses were induced only during the brief submersion in the withdrawal test, whereas sustained increases were observed during the release/swim test (Fig. 2g,h Extended Data Fig. 5e–j).

We then monitored the activity of dACC→PnC neurons during sniffing behavior (Fig. 2i). In contrast to drinking or swimming, which cause temporary pauses or delayed breathing cycles, an increase in breathing rate is accompanied by sniffing of an object (Fig. 2j,k). With the caveat that our temporal resolution (10 Hz) for identifying

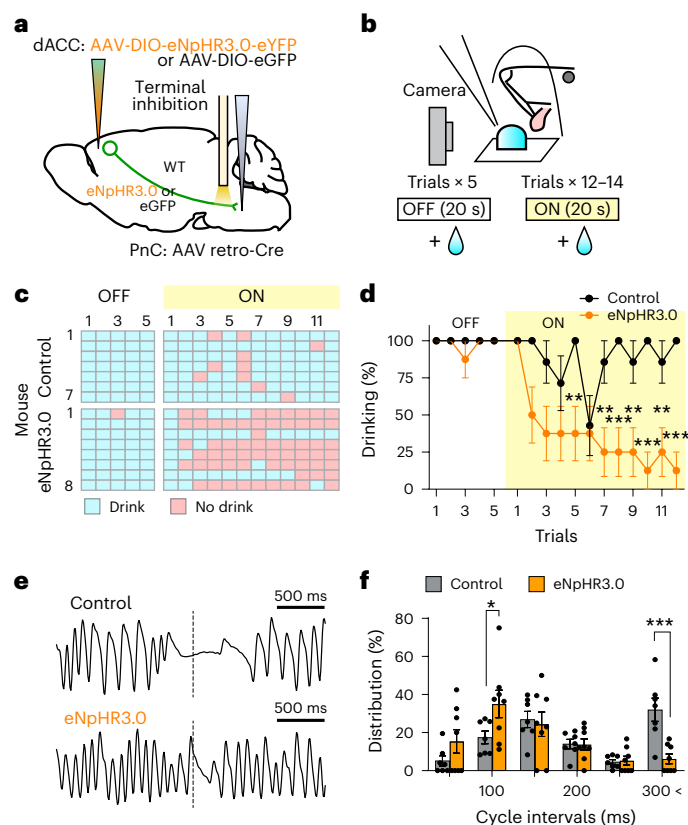


Fig. 3 | The dACC→PnC circuit is required for voluntary drinking. **a**, Schematic representation of viral injection surgery and photoinhibition targeting dACC→PnC terminals. **b**, Schematic representation of the voluntary drinking test. During the light-ON session, the presentation of water droplets was paired with dACC→PnC photoinhibition. **c,d**, Individual (**c**) or average (**d**) traces showing successful drinking responses across trials during baseline (light-OFF) and light-ON sessions (eNpHR3.0, $n = 8$; eGFP, $n = 7$ mice). **e,f**, Representative traces showing breathing cycles coordinated with drinking during light-ON session (top, control mouse; bottom, mouse expressing eNpHR3.0). Dashed lines show the moment that a water droplet was taken into the oral cavity. Scale bar, 500 ms. **f**, Percentage distribution of the intervals between breathing cycles (eNpHR3.0, $n = 8$; eGFP, $n = 7$ mice). Cycle intervals within a time frame of –100 to +500 ms from the oral intake of water were analyzed. * $P < 0.05$, ** $P < 0.01$ and *** $P < 0.001$. Data are shown as mean \pm s.e.m.

the sniffing onset was not ideal, we found that following the onset of contact-sniffing, decreased dACC→PnC neuronal activity was observed (Fig. 2k). Rebound-like activation of these neurons was observed upon the termination of sniffing (Fig. 2l). These data suggest that dACC→PnC neurons are inhibited when animals are engaged in sniffing behavior.

Taken together, concurrent antagonistic changes in breathing cycles and dACC→PnC or PnC^{GABA} activities were observed under conditions that involved voluntary behaviors, including drinking, swimming and sniffing, showing that dACC→PnC neurons respond during these behaviors.

dACC→PnC projection coordinates breathing and behavior

We next attempted to confirm that the projection from dACC→PnC neurons to the PnC itself had a role in the regulation of the previous behaviors. Mice were implanted with nasal thermistors, made to express either eNpHR3.0-eYFP or eGFP in dACC→PnC neurons (Fig. 3a and Supplementary Fig. 3a–c) and had fiber-optic cannulas implanted over the PnC. Following overnight dehydration, mice were presented with water droplets (Fig. 3b). Both eNpHR3.0 and eGFP groups drank successfully during the first session (light-off; no photoinhibition) and the first trial of the light-ON session (Fig. 3c,d). However, in subsequent

trials, the eNpHR3.0 group exhibited a decrease in drinking responses compared to controls, suggesting that inhibition of dACC→PnC projections impairs drinking (Fig. 3c,d). Drinking success rates for the eNpHR3.0 group recovered to >70% of trials by the third session in which photoinhibition ceased, and response rates for the control group remained at >80% throughout the testing session (Supplementary Fig. 3a). Light-induced changes in success rate were correlated with the level of eNpHR3.0 expression in the dACC (Supplementary Fig. 3b). We also analyzed breathing cycles during drinking behaviors using a time window of -100 to +500 ms from the oral intake of water (Fig. 3e). Compared to controls, the proportion of cycle intervals that exceeded 300 ms was significantly reduced in eNpHR3.0 mice (Fig. 3f). These results suggest that the dACC→PnC circuit may be required to coordinate breathing cycles with voluntary drinking.

Response of dACC→PnC neurons in an anxiogenic environment

Breathing can be altered according to different emotions, such as during anxiety-related states^{12–18}. We thus measured the activity of dACC→PnC neurons in anxiogenic environments.

We recorded breathing cycles and the activity of dACC→PnC neurons (as in Fig. 2a,b) while mice were placed on an elevated plus maze (EPM; Fig. 4a and Extended Data Fig. 6a). All tested mice ($n = 6$) exhibited increased breathing rate while in the exposed areas of the maze (center plate or open arms) compared to the closed arms (Fig. 4b). Consistent with our previous findings¹⁸, a correlation was found between the location of the mouse and its corresponding breathing rates. A decrease in breathing rate was observed during transitions from an exposed area to a closed arm (Fig. 4d and Extended Data Fig. 6b,c). Concurrent with these transitions (exit), increases in dACC→PnC activity were observed (Fig. 4c), revealing a correlation between slower breathing cycles and increased dACC→PnC activity (Fig. 4e). A detailed analysis of breathing phases revealed that elongation of the T_E contributed to the slower breathing rate (Extended Data Fig. 6d).

Next, we measured the activity of dACC→PnC neurons while mice freely explored an EPM. dACC→PnC neurons displayed a decrease in calcium activity as they entered the open arms of an EPM (Fig. 4f,g) in 71% of entries (37 of 52 entries), indicating that anxiogenic conditions that increase breathing rate may generally suppress the activity of dACC→PnC neurons. We then compared episodes in which the mouse either failed to fully explore the open arm of the EPM (refrained) or explored the full length of the open arm (full exploration; Fig. 4h). dACC→PnC neurons typically displayed a decrease (83% of entries) in activity upon entry of the open arm during refrained behavior (Fig. 4i). However, dACC→PnC neurons typically displayed increased activity (80% of entries) upon entry of the open arm during episodes of full exploration (Fig. 4j). Consistent with these activity patterns, breathing rates during full exploration were lower than during refrained episodes (Extended Data Fig. 6e), suggesting that these episodes were associated with decreased anxiety. These activity patterns suggest that the activity of dACC→PnC neurons is altered during the exploration of an

anxiogenic environment. An alternative explanation for the response of dACC→PnC neurons during anxiogenic conditions would be that dACC→PnC neurons were simply inhibited by negative emotional stimuli. This would predict that aversive stimuli will induce similar changes in dACC→PnC neuronal activity regardless of breathing changes. We monitored dACC→PnC neuronal responses using two paradigms that expose mice to aversive conditions—with an elevated platform (Fig. 4k) or a foot shock (Fig. 4n). Although both paradigms present aversive stimuli, they induce opposite changes in breathing rates. While a steep increase in breathing rate was seen during the elevated platform (Fig. 4l), a decrease in breathing rate was observed during foot shock (Fig. 4o,p). Specifically, during shock exposure, breathing rates slower than 300 BPM were seen during squeaking vocalization. Notably, dACC→PnC neuronal responses varied with breathing rate changes induced by each condition (Fig. 4l,m,p,q), showing an increase during slower breathing and a decrease during faster breathing. These results demonstrate that dACC→PnC neuronal responses are correlated with breathing changes and not simply responding to aversive stimuli.

dACC→PnC circuit reduces anxiety-like behaviors in mice

Given that calcium responses of dACC→PnC neurons correlated with breathing and behavioral patterns during the EPM test, we next investigated whether activation of the dACC→PnC circuit could reduce anxiety-like behaviors in mice. We used the same viral strategy as in Fig. 1d to bilaterally express ChR2 in dACC→PnC neurons (Fig. 5a and Supplementary Fig. 4a) and stimulated dACC→PnC neurons and their target projections during EPM tests (Fig. 5a–g). Photoactivation of dACC→PnC soma increased the duration spent in open arms (Fig. 5b). These results were recapitulated with terminal photostimulation of dACC terminals in the PnC (Fig. 5g and Supplementary Fig. 4d). Photostimulation of dACC terminals in the zona incerta (ZI; Fig. 5d and Supplementary Fig. 4c), a region with putative axon collaterals (Fig. 5c and Extended Data Fig. 7a), produced no notable behavioral changes (Fig. 5e). Consequently, we next examined whether the dACC→PnC projection is required for alleviating anxiety-like behavior. Mice bilaterally expressing eNpHR3.0-eYFP or eGFP in dACC→PnC neurons (Fig. 5f) were habituated beforehand to reduce baseline anxiety. Terminal photoinhibition of dACC→PnC terminals in the PnC decreased time spent in open arms (Fig. 5h), indicating that the dACC→PnC projection is required for reducing anxiety-like responses.

As a control, we performed a real-time place preference (RTPP) test (Fig. 5i,j) to measure changes in emotional valence. The same mice used in the EPM tests were exposed to 473 nm pulses or continuous 591 nm light on one side of the chamber during the second epoch of testing. Neither the ChR2 nor the eNpHR3.0 group displayed preference or aversion for the light-paired chamber (Fig. 5i,j). These results demonstrate that activation or inhibition of the dACC→PnC circuit does not induce positive or negative valence per se. As a second control test, one chamber of a two-chamber box was paired with the odor of a female cage to promote approaching behavior in male mice (Extended Data Fig. 7b,g). Male mice showed a strong preference for the odor-paired

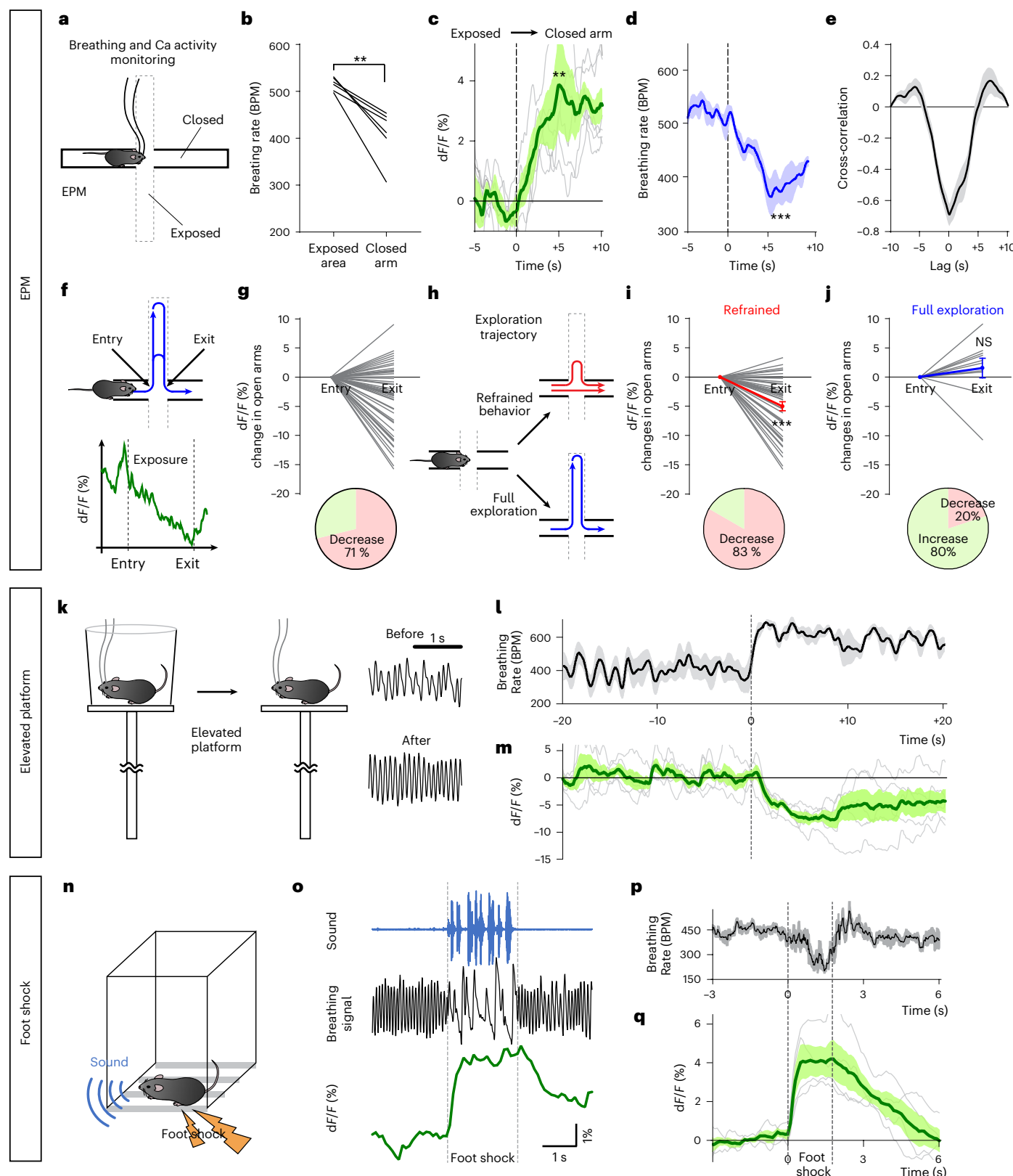
Fig. 4 | dACC→PnC activities correlate with breathing changes during aversive conditions. **a**, Simultaneous monitoring of breathing cycles and neuronal activity in an EPM. **b**, Breathing rates in exposed areas (center and open arms) and closed arms. **c**, Increases in dACC→PnC neuronal activity during exit episodes (exposed area→closed arm). **d**, Decreases in breathing rate during exit episodes. **e**, Cross-correlation between breathing rate and dACC→PnC activity during exit episodes (**b–e**, $n = 6$ mice). **f**, Schematic representation of the normalized changes in dACC→PnC activity based on calcium levels during open arm entry and exit. **g**, Normalized changes in dACC→PnC activity during open arm exposure ($n = 52$ episodes, in 6 mice). Decreases in dACC→PnC response were observed in 71% (37 of 52) of episodes. **h**, Depiction of exploratory behavioral patterns in an exposed area. **i,j**, Normalized changes in dACC→PnC activity associated with refrained behaviors (**i**, $n = 42$ episodes) and full exploration of

open arms (**j**, $n = 10$ episodes). **k**, Schematic representation of elevated platform exposure (left) and raw traces showing breathing signals (right). Scale bar, 1 s. **l,m**, Average traces ($n = 5$ mice) showing changes in breathing rate (**l**) and dACC→PnC activity (**m**) in response to elevated platform exposure. Dashed vertical lines represent the time of cylinder opening. **n**, Schematic representation of foot shock exposure. Vocal sounds generated by mice were simultaneously recorded. **o**, Representative traces showing sound waveform (top), raw breathing traces (middle) and dACC→PnC calcium activity (bottom). Dashed vertical lines represent the time of foot shock delivery. **p,q**, Average traces ($n = 4$ mice) showing the changes in breathing rate (**p**) and dACC→PnC calcium activity (**q**) during the exposure to foot shock. Dashed vertical lines represent the time of foot shock delivery. ** $P < 0.01$ and *** $P < 0.001$. Data are shown as mean ± s.e.m. Gray lines (**c,m,q**) show individual traces from each animal.

chamber, but neither the ChR2 nor the eNpHR3.0 groups displayed behavioral changes compared to controls (Extended Data Fig. 7b,g), showing that approach responses are not altered by manipulation of the dACC→PnC projection. The same mice were also placed in a chamber equipped with 2,4,5-trimethylthiazoline (TMT; fox anogenital odor), which provokes avoidance behavior. During photostimulation, a

reduction of avoidance responses was observed in the ChR2-expressing group (Extended Data Fig. 7c). A further increase in avoidance response was not observed in the eNpHR3.0-expressing group, perhaps due to a saturated response at the baseline (Extended Data Fig. 7h).

We then examined the function of the dACC→PnC projection using another anxiogenic paradigm, a light/dark choice test, where



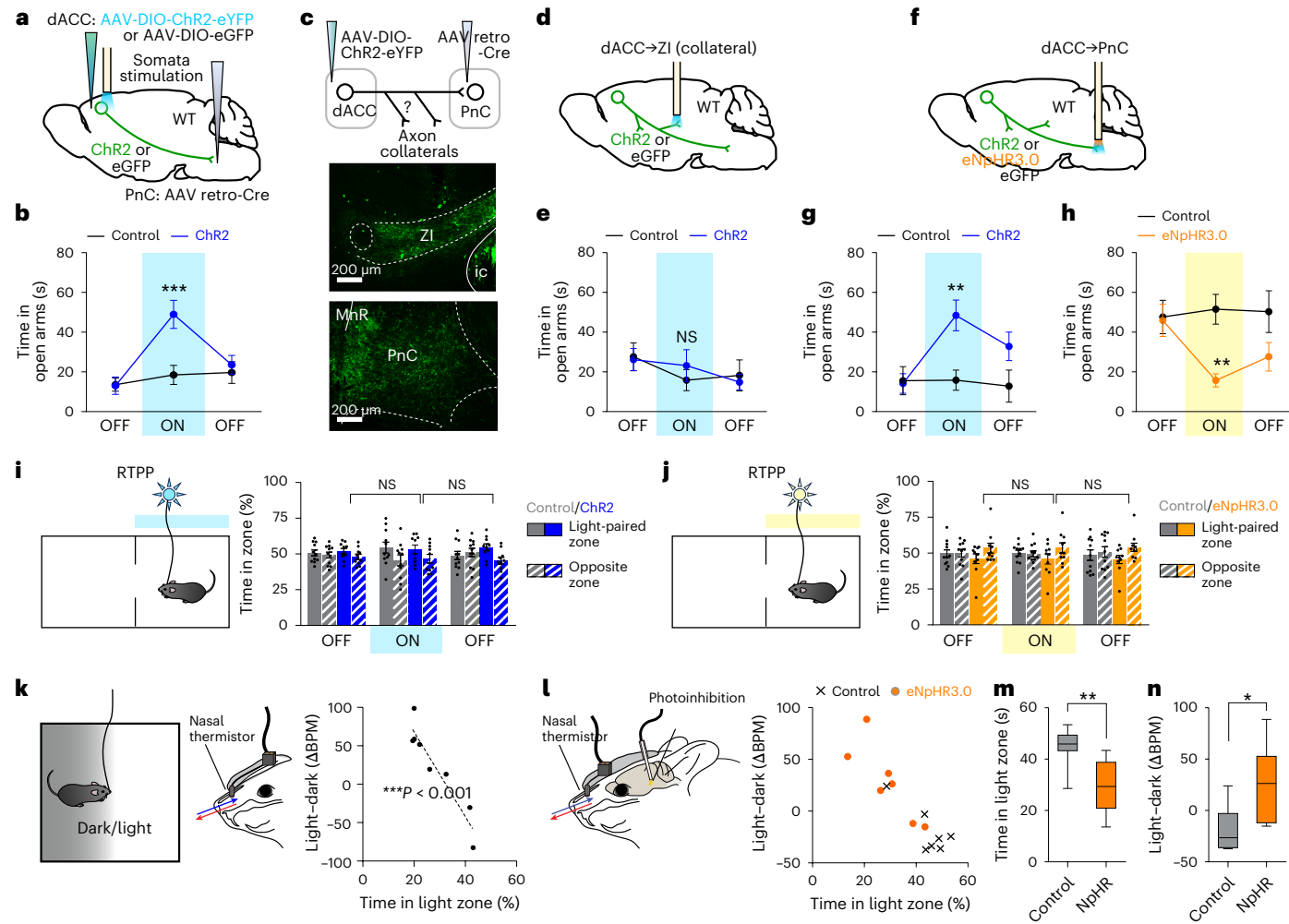


Fig. 5 | dACC→PnC activation reduces breathing rate and anxiety-like behaviors. **a**, Schematic representation showing photoactivation of dACC→PnC neurons expressing ChR2-eYFP. **b**, Photoactivation of dACC→PnC neurons increased time spent in open arms during an EPM test (ChR2, $n=10$; eGFP, $n=11$ mice). **c**, Top: schematic representation of the viral injection surgery and observation of axon collaterals. Bottom: microscopic images showing eYFP-labeled terminals in the ZI and PnC. Scale bars, 200 μm. **d**, Photoactivation targeting the collaterals in the ZI. **e**, Photoactivation of dACC→ZI collaterals did not change time spent in the open arms during an EPM test (ChR2, $n=8$; eGFP, $n=7$ mice). **f**, Photoactivation or inhibition targeting dACC→PnC projections. **g**, Photoactivation of dACC→PnC projections increased time spent in open arms during an EPM test (ChR2, $n=7$; eGFP, $n=7$ mice). **h**, Photoinhibition of dACC→PnC projections decreased time spent in open arms during an EPM test (eNpHR3.0, $n=10$; eGFP, $n=11$ mice). **i**, Photoactivation of dACC→PnC neurons

does not induce RTPP or aversion (ChR2, $n=10$; eGFP, $n=11$ mice). **j**, Photoinhibition of dACC→PnC projections does not induce RTPP or aversion (eNpHR3.0, $n=10$; eGFP, $n=11$ mice). **k**, Light/dark choice test with breathing monitoring using a nasal thermistor. Right: time spent in the light zone was correlated with increases in ΔBPM (light–dark). **l**, Light/dark choice test performed with breathing monitoring and photoinhibition of dACC→PnC projections. Right: plot showing the time spent in the light zone and breathing rate differences (eNpHR3.0, $n=7$; eGFP, $n=8$ mice). **m,n**, Photoinhibition of dACC→PnC projections decreases time spent in the light zone (**m**) and increases breathing rate changes (light–dark, ΔBPM; **n**). $P>0.05$ considered not significant (NS), $*P<0.05$, $**P<0.01$ and $***P<0.001$. Line and bar graphs are shown as mean \pm s.e.m. Box-whisker plots are shown as median and interquartile range with minimum and maximum. MnR, median raphe nucleus; ic, internal capsule.

time spent in the light zone was measured. Mice were implanted with nasal thermistors (Fig. 5k), and the breathing rates of mice in light and dark zones were measured. A strong inverse correlation was observed between an increase in breathing rate (ΔBPM; light–dark) and the behavioral response of mice (time in the light zone; Fig. 5k, right), suggesting that elevations in breathing rates are associated with higher anxiety-like responses (decreased time in the light zone). Using mice expressing eNpHR3.0, ChR2 or eGFP, we monitored breathing rate and behavioral responses during a light/dark choice test while pairing the light zone with 591-nm or 473-nm stimulation (Fig. 5l). Mice expressing eNpHR3.0 had increased ΔBPM (light–dark) and spent less time in the light zone (Fig. 5l–n) compared to controls. Conversely, the ChR2-expressing group had reduced ΔBPM (light–dark) and spent an

increased time in the light zone (Extended Data Fig. 7d–f) compared to controls. These results hint at the possibility that modulation of breathing rates by the dACC→PnC projection is associated with the modulation of anxiety-like responses.

Breathing and anxiety modulation via dACC→PnC→VLM circuit

Next, we explored whether the influence of PnC on breathing rate and anxiety could be dissociated at the downstream level or not. To characterize efferent projections of inhibitory PnC neurons, we injected AAV-DIO-ChR2-eYFP into the PnC of *Vgat-ires-Cre* mice (Fig. 6a). The densest signals were found in breathing-related regions in the medullary area, covering the dorsolateral medulla and VLM and the

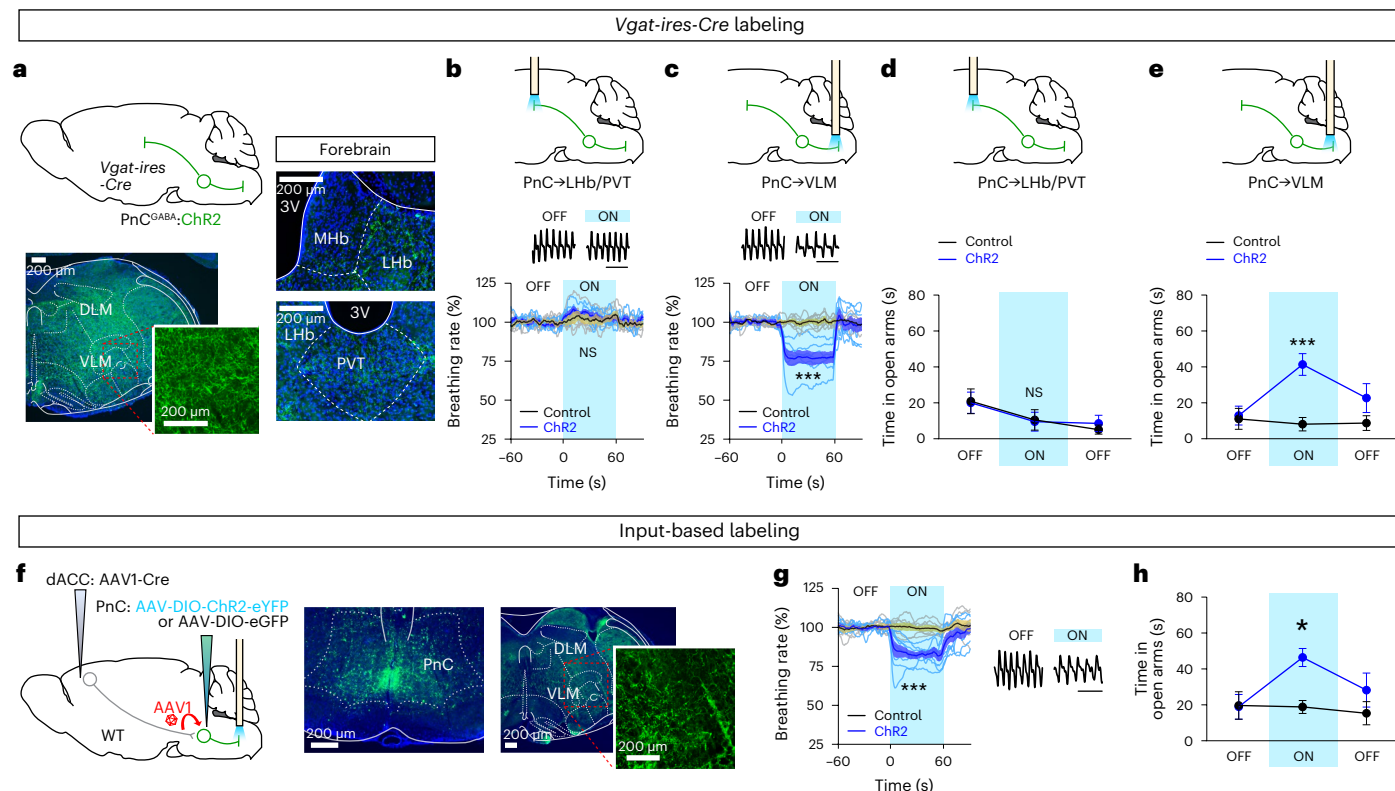


Fig. 6 | PnC^{GABA}→VLM activation attenuates breathing rate and anxiety-like behavior. **a**, Projections of PnC^{GABA} neurons in the medulla (left) and forebrain regions (right). Scale bars, 200 μm. **b,c**, Monitoring of breathing rates using inductance plethysmography under anesthesia with photoactivation targeting either the PnC→forebrain (**b**, LHb/PVT; ChR2, $n = 7$; eGFP, $n = 8$ mice) or the PnC→VLM projection (**c**, ChR2, $n = 7$; eGFP, $n = 7$ mice). **d**, Photoactivation targeting PnC→forebrain (LHb/PVT) terminals did not alter time spent in open arms during an EPM test ($n = 7$; eGFP, $n = 8$ mice). **e**, Photoactivation targeting PnC→VLM terminals increased time spent in open arms during an EPM test

($n = 7$; eGFP, $n = 7$ mice). **f**, Left: schematic representation of the viral injection surgery for anterograde labeling of PnC neurons and terminal stimulation targeting the VLM. Right: microscopic images show DIO-ChR2 expression in the PnC area and terminals in the VLM. Scale bars, 200 μm. **g,h**, Photoactivation of dACC→PnC→VLM terminals induces a decrease in breathing rate (**g**) and increases time spent in open arms during an EPM test (**h**; ChR2, $n = 8$; eGFP, $n = 7$ mice). $P > 0.05$ considered not significant (NS), * $P < 0.05$ and *** $P < 0.001$. Data are shown as mean \pm s.e.m. DLM, dorsolateral medulla; 3V, third ventricle; MHb, medial habenula.

parabrachial nucleus of the pons (Fig. 6a and Extended Data Fig. 8a,b). Additionally, a few forebrain regions, including the lateral habenula (LHb), the paraventricular thalamic nucleus (PVT) and the bed nucleus of stria terminalis, exhibited eYFP-labeled terminals with lower intensities (Extended Data Fig. 8a).

Photostimulation of PnC^{GABA}→VLM projections lowered breathing rates as measured by inductance plethysmography under anesthesia, whereas no change was observed in eGFP controls (Fig. 6c, Extended Data Fig. 9a,b and Supplementary Fig. 5b). However, photostimulation of PnC^{GABA} terminals in the LHb/PVT had no effect on breathing rate (Fig. 6b, Extended Data Fig. 9c-f and Supplementary Fig. 5a). Next, we examined the effect of photostimulating PnC^{GABA}→VLM and PnC^{GABA}→Lhb/PVT projections on anxiety-like responses during an EPM test. Photostimulation of the PnC→VLM projection led to increased exploration of open arms compared to controls (Fig. 6e), whereas no notable behavioral changes were induced by photostimulation of the PnC^{GABA}→Lhb/PVT projection (Fig. 6d).

Finally, to test the dACC→PnC→VLM circuit, we bilaterally injected AAV1-Cre into the dACC, bilaterally injected DIO-ChR2 or eGFP into the PnC and implanted optic fibers over the VLM (Fig. 6f and Supplementary Fig. 5c). Photostimulation of terminals in the VLM decreased breathing rate (measured by inductance plethysmography under anesthesia; Fig. 6g and Extended Data Fig. 9g) and increased time spent in the open arms of an EPM (Fig. 6h). Taken together, these results establish a role for the dACC→PnC→VLM circuit in slowing breathing rate and reducing anxiety-like behaviors.

Discussion

To date, cellular and circuit-level analyses of respiratory regulation have largely been confined to brainstem networks and ascending inputs from the spinal cord^{2,3,45}. However, compared to the well-characterized role of the brainstem, how cortical circuits and their brainstem projections modulate breathing rhythms hitherto remains poorly understood. Our study demonstrates a top-down brain circuit for the inhibitory control of breathing, which is important for coordinating breathing with behavior and emotional states.

Although we identified the dACC→PnC projection as being a substrate for mediating top-down control of breathing, this does not exclude the possibility of other circuits that can engage with PnC^{GABA} neurons. Indeed, we note that whereas photostimulation of PnC^{GABA} neurons produced rapid decreases in breathing rate, photoactivation of dACC→PnC neurons produced more gradual changes, which may hint at the existence of other nodes upstream of PnC^{GABA} neurons, whose concurrent activation is also required to produce sharper decreases in breathing rate.

Although calcium activity was seen in dACC→PnC and PnC^{GABA} neurons whenever the breathing rate decreased, it is notable that these signals were preceded by breathing rate changes whenever the breathing rate was increased. This suggests that although they may be causally involved in slowing breathing, the activity seen during bouts of faster breathing may be more correlational and likely involve other mechanisms or circuits that, in turn, partly mediate their effects via inhibition of dACC→PnC and PnC^{GABA} neurons.

Heightened breathing rate and hyperventilation are prevailing symptoms of environmental stress across species^{12,15–18} and widely observed in panic and anxiety-related disorders in humans^{12–15}. By contrast, slow breathing, altered breathing patterns (such as an emphasis on longer exhalation or box breathing) and mindfulness skills are practiced for controlling emotions^{19–21}. While the precise mechanisms by which slow breathing practices influence the internal state of the brain remain unknown, theories have been proposed. One line of inquiry explores changes in bodily states and feedback interoception, where longer expiration leads to a decreased heart rate via respiratory sinus arrhythmia^{46–48}, which in turn affects the interoception of the heart rate^{49,50}. Another line of research explores the role of brainstem breathing centers themselves. In this context, it is worth noting the projection from inhibitory PnC neurons to the parabrachial nucleus, where *Oprm1*⁺ neurons have been shown to reduce stress-induced increases in breathing rate when chemogenetically inhibited¹⁸. Whether PnC neurons indeed project to parabrachial *Oprm1*⁺ neurons and whether they can recapitulate the effects seen from PnC→VLM photostimulation remain to be seen. Additionally, subpopulations of *Cdh9*/*Dbx1*-expressing neurons in the pre-Bötzinger complex project to the locus coeruleus and respond to the inspiratory phase of breathing. Their ablation leads to reduced breathing rates, grooming and arousal in mice, thus raising the possibility that the dACC→PnC→VLM circuit identified here converges on *Cdh9*/*Dbx1*⁺ neurons, where their inhibition would be expected to both slow breathing and produce anxiolytic effects. What functional differences or redundancies exist between these pontine and medullary projections of the PnC also warrant future inquiry. It is also interesting to note that the emotional effects seen from activating the PnC→VLM projection were strongly coupled with the respiratory effects, suggesting that slow breathing in itself may be the mechanistic cause for reducing anxiety-like responses. This conclusion is also supported by the finding that dACC→PnC neuronal activity is increased in neutral situations that require delayed breathing, demonstrating that these neurons are unlikely to mediate general anxiety.

Finally, our results also illustrate a bidirectional relationship between emotional state and breathing influencing each other. Decreases in the dACC→PnC neuronal activity were observed under anxiogenic conditions, including during the exploration of open arms or exposure to an elevated platform, suggesting that anxiogenic situations can increase breathing rate in part via inhibition of this slow breathing circuit. Conversely, direct inhibition of this circuit, which leads to faster breathing, also results in an increase in anxiety-like responses. This suggests a complex process of feedforward cycles rather than a simple linear process, whereby anxiety or stress response leads to faster breathing, which then exacerbates anxiety. Such findings may have implications for situations where hyperventilation is accompanied by anxiety, such as panic, and might help in our understanding of methods that reduce anxiety-related responses through voluntary slow breathing.

Online content

Any methods, additional references, Nature Portfolio reporting summaries, source data, extended data, supplementary information, acknowledgements, peer review information; details of author contributions and competing interests; and statements of data and code availability are available at <https://doi.org/10.1038/s41593-024-01799-w>.

References

- Feldman, J. L., Mitchell, G. S. & Nattie, E. E. Breathing: rhythmicity, plasticity, chemosensitivity. *Annu. Rev. Neurosci.* **26**, 239–266 (2003).
- Del Negro, C. A., Funk, G. D. & Feldman, J. L. Breathing matters. *Nat. Rev. Neurosci.* **19**, 351–367 (2018).
- Dick, T. E. et al. Facts and challenges in respiratory neurobiology. *Respir. Physiol. Neurobiol.* **258**, 104–107 (2018).
- Pagliardini, S., Funk, G. D. & Dickson, C. T. Breathing and brain state: urethane anesthesia as a model for natural sleep. *Respir. Physiol. Neurobiol.* **188**, 324–332 (2013).
- Arthurs, J. W., Bowen, A. J., Palmiter, R. D. & Baertsch, N. A. Parabrachial tachykinin-1-expressing neurons involved in state-dependent breathing control. *Nat. Commun.* **14**, 963 (2023).
- Park, H.-D. et al. Breathing is coupled with voluntary action and the cortical readiness potential. *Nat. Commun.* **11**, 289 (2020).
- Betka, S., Adler, D., Similowski, T. & Blanke, O. Breathing control, brain, and bodily self-consciousness: toward immersive digiceuticals to alleviate respiratory suffering. *Biol. Psychol.* **171**, 108329 (2022).
- Moore, J. D. et al. Hierarchy of orofacial rhythms revealed through whisking and breathing. *Nature* **497**, 205–210 (2013).
- Hegland, K. W., Bolser, D. C. & Davenport, P. W. Volitional control of reflex cough. *J. Appl. Physiol.* **113**, 39–46 (2012).
- Watanabe, Y., Abe, S., Ishikawa, T., Yamada, Y. & Yamane, G. Y. Cortical regulation during the early stage of initiation of voluntary swallowing in humans. *Dysphagia* **19**, 100–108 (2004).
- Martin-Harris, B. Coordination of respiration and swallowing. *GI Motility online* <https://www.nature.com/gimo/contents/pt1/full/gimo10.html> (2006).
- Homma, I. & Masaoka, Y. Breathing rhythms and emotions. *Exp. Physiol.* **93**, 1011–1021 (2008).
- Holt, P. E. & Andrews, G. Hyperventilation and anxiety in panic disorder, social phobia, GAD and normal controls. *Behav. Res. Ther.* **27**, 453–460 (1989).
- Leander, M. et al. Impact of anxiety and depression on respiratory symptoms. *Respir. Med.* **108**, 1594–1600 (2014).
- Masaoka, Y., Jack, S., Warburton, C. J. & Homma, I. Breathing patterns associated with trait anxiety and breathlessness in humans. *Jpn. J. Physiol.* **54**, 465–470 (2004).
- Bondarenko, E., Hodgson, D. & Nalivaiko, E. Prelimbic prefrontal cortex mediates respiratory responses to mild and potent prolonged, but not brief, stressors. *Respir. Physiol. Neurobiol.* **204**, 21–27 (2014).
- Bondarenko, E. & Nalivaiko, E. Pharmacological inhibition of infralimbic prefrontal cortex abolishes sniffing behavior and respiratory response to stress. *FASEB J.* **30**, 1261 (2016).
- Liu, S. et al. Divergent brainstem opioidergic pathways that coordinate breathing with pain and emotions. *Neuron* **110**, 857–873 (2022).
- Valenza, M. C. et al. Effectiveness of controlled breathing techniques on anxiety and depression in hospitalized patients with COPD: a randomized clinical Trial. *Respir. Care* **59**, 209–215 (2014).
- Strigo, I. A. & Craig, A. D. Interoception, homeostatic emotions and sympathovagal balance. *Philos. Trans. R. Soc. Lond. B* **371**, 20160010 (2016).
- Balban, M. Y. et al. Brief structured respiration practices enhance mood and reduce physiological arousal. *Cell Rep. Med.* **4**, 100895 (2023).
- Herrero, J. L., Khuvis, S., Yeagle, E., Cerf, M. & Mehta, A. D. Breathing above the brain stem: volitional control and attentional modulation in humans. *J. Neurophysiol.* **119**, 145–159 (2018).
- Mckay, L. C., Evans, K. C., Frackowiak, R. S. & Corfield, D. R. Neural correlates of voluntary breathing in humans. *J. Appl. Physiol.* **95**, 1170–1178 (2003).
- Tremouereux, L. et al. Does the supplementary motor area keep patients with Ondine's curse syndrome breathing while awake? *PLoS ONE* **9**, e84534 (2014).
- Macey, K. E. et al. Inspiratory loading elicits aberrant fMRI signal changes in obstructive sleep apnea. *Respir. Physiol. Neurobiol.* **151**, 44–60 (2006).

26. Davenport, P. W. & Vovk, A. Cortical and subcortical central neural pathways in respiratory sensations. *Respir. Physiol. Neurobiol.* **167**, 72–86 (2009).
27. Liotti, M. et al. Brain responses associated with consciousness of breathlessness (air hunger). *Proc. Natl Acad. Sci. USA* **98**, 2035–2040 (2001).
28. Harper, R. M. et al. Hypercapnic exposure in congenital central hypoventilation syndrome reveals CNS respiratory control mechanisms. *J. Neurophysiol.* **93**, 1647–1658 (2005).
29. Evans, K. C. et al. BOLD fMRI identifies limbic, paralimbic, and cerebellar activation during air hunger. *J. Neurophysiol.* **88**, 1500–1511 (2002).
30. Kelly, B. N., Huckabee, M. L., Jones, R. D. & Carroll, G. J. The influence of volition on breathing-swallowing coordination in healthy adults. *Behav. Neurosci.* **121**, 1174–1179 (2007).
31. Jürgens, U. Neural pathways underlying vocal control. *Neurosci. Biobehav. Rev.* **26**, 235–258 (2002).
32. Biskamp, J., Bartos, M. & Sauer, J.-F. Organization of prefrontal network activity by respiration-related oscillations. *Sci. Rep.* **7**, 45508 (2017).
33. Karalis, N. & Sirota, A. Breathing coordinates cortico-hippocampal dynamics in mice during offline states. *Nat. Commun.* **13**, 467 (2022).
34. Baertsch, N. A., Baertsch, H. C. & Ramirez, J. M. The interdependence of excitation and inhibition for the control of dynamic breathing rhythms. *Nat. Commun.* **9**, 843 (2018).
35. Hirrlinger, J. et al. GABA-glycine cotransmitting neurons in the ventrolateral medulla: development and functional relevance for breathing. *Front. Cell. Neurosci.* **13**, 517 (2019).
36. Sherman, D., Worrell, J. W., Cui, Y. & Feldman, J. L. Optogenetic perturbation of preBötzinger complex inhibitory neurons modulates respiratory pattern. *Nat. Neurosci.* **18**, 408–414 (2015).
37. Hülsmann, S., Hagos, L., Eulenburg, V. & Hirrlinger, J. Inspiratory off-switch mediated by optogenetic activation of inhibitory neurons in the preBötzinger complex in vivo. *Int. J. Mol. Sci.* **22**, 2019 (2021).
38. Yang, C. F., Kim, E. J., Callaway, E. M. & Feldman, J. L. Monosynaptic projections to excitatory and inhibitory preBötzinger complex neurons. *Front. Neuroanat.* **14**, 58 (2020).
39. Zingg, B. et al. AAV-mediated anterograde transsynaptic tagging: mapping corticocollicular input-defined neural pathways for defense behaviors. *Neuron* **93**, 33–47 (2017).
40. Zingg, B., Peng, B., Huang, J., Tao, H. W. & Zhang, L. I. Synaptic specificity and application of anterograde transsynaptic AAV for probing neural circuitry. *J. Neurosci.* **40**, 3250–3267 (2020).
41. Scott, G., Westberg, K.-G., Vrentzos, N., Kolta, A. & Lund, J. Effect of lidocaine and NMDA injections into the medial pontobulbar reticular formation on mastication evoked by cortical stimulation in anaesthetized rabbits. *Eur. J. Neurosci.* **17**, 2156–2162 (2003).
42. McAfee, S. S. et al. Minimally invasive highly precise monitoring of respiratory rhythm in the mouse using an epithelial temperature probe. *J. Neurosci. Methods* **263**, 89–94 (2016).
43. Liu, S. & Han, S. Simultaneous recording of breathing and neural activity in awake behaving mice. *STAR Protoc.* **3**, 101412 (2022).
44. Huckabee, M. L., Deecke, L., Cannito, M. P., Gould, H. J. & Mayr, W. Cortical control mechanisms in volitional swallowing: the Bereitschaftspotential. *Brain Topogr.* **16**, 3–17 (2003).
45. Le Gal, J. P. et al. Modulation of respiratory network activity by forelimb and hindlimb locomotor generators. *Eur. J. Neurosci.* **52**, 3181–3195 (2020).
46. Fanning, J. et al. Relationships between respiratory sinus arrhythmia and stress in college students. *J. Behav. Med.* **43**, 308–317 (2020).
47. Manuel, J. et al. Deciphering the neural signature of human cardiovascular regulation. *eLife* **9**, e55316 (2020).
48. Menuet, C. et al. PreBötzinger complex neurons drive respiratory modulation of blood pressure and heart rate. *eLife* **9**, e57288 (2020).
49. Molle, L. & Coste, A. The respiratory modulation of interoception. *J. Neurophysiol.* **127**, 896–899 (2022).
50. Klein, A. S., Dolensek, N., Weiand, C. & Gogolla, N. Fear balance is maintained by bodily feedback to the insular cortex in mice. *Science* **374**, 1010–1015 (2021).

Publisher's note Springer Nature remains neutral with regard to jurisdictional claims in published maps and institutional affiliations.

Springer Nature or its licensor (e.g. a society or other partner) holds exclusive rights to this article under a publishing agreement with the author(s) or other rightsholder(s); author self-archiving of the accepted manuscript version of this article is solely governed by the terms of such publishing agreement and applicable law.

© The Author(s), under exclusive licence to Springer Nature America, Inc. 2024

Methods

Animals

All procedures for animal surgical and behavioral experiments (protocol 16-00020) were approved by the Institutional Animal Care and Use Committee of the Salk Institute according to National Institutes of Health guidelines. Wild-type or *Vgat-ires-Cre* knock-in (Jackson Laboratories, 028862) mouse lines, in adulthood (2–4 months) of both sexes, on a C57Bl/6 background were group housed on a 12-h light/12-h dark cycle under constant temperature (20–21 °C) and humidity (60–70%) conditions, and provided with food and water ad libitum.

Respiratory measurements

Inductance plethysmography. Pressure signals generated by respiratory thoracic movements were converted into voltage signals by a piezoelectric sensor placed beneath the chest of mice under isoflurane-induced anesthesia. Mice were initially exposed to 3% isoflurane. The mice were placed in a stereotaxic frame 5–10 s after the loss of movement. Isoflurane (delivered through the nasal cone of the stereotaxic device) was adjusted to 0.8–1% or 1.2–1.5% to induce light (~200 BPM) or deep (~150 BPM) anesthesia. The piezoelectric sensor was connected to a PowerLab monitoring system (PL3504), which was operated by LabChart 8 Pro software (ADIInstruments). LabChart 8 Pro software was used for the sampling of voltage signals, signal processing, detection of breathing cycles and calculation of breathing rate. Data were sampled at 400 Hz, low-pass filtered at 10 Hz and smoothed with a 100-ms window.

Nasal thermistor recording. Nasal thermistor-based breathing monitoring was performed as previously described^{18,42,43}. A custom sensor was built with a negative temperature coefficient thermistor (TE Connectivity) and an interconnector (Mill-Max) and stereotactically implanted into the nasal cavity of mice, ~1 mm ventral from the skull surface. The interconnector was attached to an electric patch cord, which was connected to a rotary joint with a voltage divider (Phidgets), which in turn was connected to a PowerLab device. Data were sampled at 1 kHz, filtered with a 0.4–25 Hz band-pass filter and smoothed with a 50-ms moving window. Breathing cycles, rate and estimated amplitude were calculated by the LabChart Pro 8 software, and peak detection was validated with manual observation.

Breathing measurements with facial (jaw) recording. For recording under anesthesia (maintained at 0.8–1.0% isoflurane), mice were fixed in a stereotaxic frame with a transparent cylindrical mask (3 cm diameter), and orofacial behaviors were recorded at 25 Hz. For awake condition recording, mice were implanted with nasal thermistor sensors. On testing days, mice were placed in a glass cylinder (15 cm height and 19.5 cm diameter), habituated for 40 min and tested with optogenetic stimulations at 25 Hz.

Stereotaxic surgery

Mice were anesthetized with isoflurane (4% initial and 1.5% for maintenance) and fixed on a stereotaxic frame (David Kopf Instruments) equipped with a heating pad. The skull was drilled with a handpiece drill (Foredom). Viral solutions or CTB tracer were loaded into glass pipettes filled with mineral oil and then injected into target brain coordinates at 1 nl s⁻¹ rate using a Nanoject III injector (Drummond Scientific). Target coordinates (relative to bregma) for virus and CTB tracer injections were anterior–posterior (AP), +1.2 mm; medial–lateral (ML), ±0.5 mm; dorsal–ventral (DV), -1.2 mm for the dACC and +AP, -5.0 mm; ML, +1.8 mm; and DV, -5.4 mm, at a 15° angle, for the PnC.

For optogenetic experiments on dACC→PnC neurons, 400 nl of AAVDJ-EF1a-DIO-hChR2-eYFP-WPRE-pA (1.2×10^{12} genome copies (GC) per ml), AAV5-EF1a-DIO-eNpHR3.0-eYFP-WPRE-pA (6.1×10^{12} GC per ml) or control AAVDJ-syn-DIO-eGFP (2.3×10^{12} GC per ml) was injected into the dACC, and 200-nl solution of AAV retrograde-EF1a-Cre-WPRE-pA

(3.2×10^{13} GC per ml) was injected into the PnC. Two fiber-optic cannulas (200 μm core diameter, numerical aperture (NA) = 0.22) were implanted bilaterally over the dACC ($\pm 2^\circ$ angle; AP, +1.2 mm; ML, ±0.6 mm; DV, -1.2 mm) for soma stimulation. For terminal experiments, fiber-optic cannulas (200 μm core diameters, NA = 0.22) were implanted bilaterally over the ZI (AP, -1.8 mm; ML, ±1.2 mm; DV, -4.3 mm) or unilaterally over the PnC (AP, -5.0 mm; ML, +0.4 mm; DV, -5.0 mm).

For optogenetic experiments on PnC^{GABA} neurons and their terminals, 300 nl of AAVDJ-EF1a-DIO-hChR2-eYFP-WPRE-pA, AAV5-EF1a-DIO-eNpHR3.0-eYFP-WPRE-pA or AAVDJ-syn-DIO-eGFP was injected into the PnC in *Vgat-ires-Cre* transgenic mice. For PnC soma stimulation, fiber-optic cannulas (200 μm core diameter, NA = 0.22) were implanted over the PnC (AP, -5.0 mm; ML, +0.4 mm; DV, -5.0 mm). For terminal stimulation, fiber-optic cannulas (200 μm core diameter, NA = 0.22) were implanted over the LHB/PVT ($\pm 15^\circ$ angle; AP, -1.4 mm; ML, ±1.25 mm; DV, -3.0 mm) or the VLM (AP, -2.5 mm from λ, ML, +1.3 mm; DV, -4.8 mm).

For jGCaMP7s experiments on dACC→PnC neurons, 400 nl of AAV1-syn-FLEX-jGCaMP7s-WPRE (1.5×10^{13} GC per ml) was injected into the right dACC, and 200 nl solution of AAV retrograde-EF1a-Cre-WPRE-pA was injected into the PnC. A fiber-optic cannula (400 μm core diameter, NA = 0.5) was implanted over the dACC (AP, +1.2 mm; ML, +0.5 mm; DV, -1.2 mm). For jGCaMP7s experiments on PnC^{GABA} neurons, 300 nl of AAV1-syn-FLEX-jGCaMP7s-WPRE was injected into the right PnC, and a fiber-optic cannula (400 μm core diameter, NA = 0.5) was implanted over the PnC (AP, -5.0; ML, +0.4 mm; DV, -5.0 mm).

For anterograde labeling of PnC neurons for immunohistochemistry, 400 nl of AAV1-syn-Cre-WPRE-pA (3.4×10^{13} GC per ml) was injected into the right dACC, and 300 nl of AAVDJ-syn-DIO-eGFP was injected into the PnC. Eight weeks after injection, mice were killed by transcardial perfusion.

For anterograde labeling of PnC neurons for optogenetic experiments, 400 nl of AAV1-syn-Cre-WPRE-pA (3.4×10^{13} GC per ml) was injected bilaterally into the dACC, and 300 nl of AAVDJ-EF1a-DIO-hChR2-eYFP-WPRE-pA or AAVDJ-syn-DIO-eGFP was injected bilaterally into the PnC. Fiber-optic cannulas (200 μm core diameter, NA = 0.22) were implanted into the right VLM.

For retrograde tracing experiments using CTB, 200 nl of CTB-Alexa Fluor 555 was injected into the PnC or dACC. Seven to ten days after injection, mice were killed by transcardial perfusion.

Optogenetic stimulation

A 470-nm collimated diode and a 589-nm diode-pumped solid-state laser were used for the optogenetic activation and inhibition experiments, respectively. Photoactivation with 470-nm light pulses (20 Hz, 5-ms pulse width and ~9 mW intensity at the fiber tip) was delivered through a patch cord connected to the fiber-optic cannula. Approximately 9 mW stimulation was used for all photoactivation experiments unless otherwise noted. Photoactivation of PnC→LHB/PVT and PnC→VLM terminals during EPM tests was performed with 15-Hz stimulation. Photoinhibition with continuous light (589 nm, ~6 mW at the fiber tip) was delivered through a patch cord connected to the fiber-optic cannula.

Fiber photometry

A dual-wavelength fiber-photometry system (Doric Lenses) was assembled with a dichroic mini cube (iFMC4), 405-nm and 465-nm connectorized LEDs, a fluorescence detector/amplifier and a pyPhotometry controller board (1.0.2) operated by Python script provided by pyPhotometry. Calcium-dependent fluorescence (465-nm excitation; F_{465}) and isosbestic control fluorescence (405-nm excitation; F_{405}) were monitored at 130 Hz using interleaved excitation. Data were analyzed by a custom-built LabView VI. Isosbestic F_{405} fluorescence was fitted to F_{465} signals by least mean squares fitting (F_{405}^{fitted}). Motion-corrected fluorescence signal (dF/F) was calculated by the following

formula: $(F_{465} - F_{405}^{\text{fitted}})/F_{405}^{\text{fitted}}$. Breathing monitoring (PowerLab) and fiber-photometry systems were synchronized with a TTL signal generated by a cDAQ output device (National Instruments, NI-9401) or a Raspberry Pi 4B device.

Voluntary drinking

Before the experiment, mice were water-deprived overnight. Then they were tethered to an electric cord and an optical patch cord for monitoring breathing and calcium signals, respectively, and placed in a cylindrical chamber (15 cm height and 11 cm diameter). A 10- μl water bolus (droplet) was provided through a small hole (~1.5 cm diameter) using a micropipette. Before the testing session, mice were acclimated to the cylinder for 2 min and given five displays of 10- μl water droplets. In a 10-min testing session, water droplets were given for 20 s, 5 times without photostimulation (light-off session; baseline response). Water droplets were then given for 20 s, 12 times with photostimulation (light-ON session). On the third session (light-off), water droplets were given for 20 s, 12 times, without photostimulation. Water droplets were given at an interval spaced between 5 and 30 s apart. Videos were recorded at 25 Hz. Peri-event analysis (breathing and calcium signals) was performed relative to the video frame where the water bolus entered the mouth of the mouse.

Swimming

Before exposure to water (25 °C, 12 cm depth and 15 cm diameter cylinder), electric and optical connections were thoroughly covered with a hydrophobic jelly (Vaseline). Mice were lifted by their tail and slowly descended into the water until their lower face and upper limbs were submerged. For withdrawal experiments, mice were lifted out after 1–2 s of brief submersion. For release/swimming experiments, mice were gently released and allowed to swim for 30–60 s. Behavior was video-recorded from the side at 10 Hz.

Foot shock

Mice were tethered to electric and optical patch cords (for breathing monitoring and photostimulation, respectively) and placed in a chamber ($W \times D \times H = 26 \times 30 \times 33 \text{ cm}$; Med Associates) equipped with an electric grid floor. Behavior was video-recorded from the top at 10 Hz, and sound was recorded at 22 kHz. During the experiment, mice received four electric foot shocks (2 s, 0.3 mA) with 30–60 s intertrial intervals. The sound file (.wav) was high pass filtered at 7 kHz to remove background noise, allowing for the extraction of squeaking vocalization.

Object sniffing

Mice were tethered to electric and optical patch cords and placed in a cage with fresh cage bedding ($W \times D \times H = 29 \times 18 \times 13 \text{ cm}$). After an acclimation period of 3 min, a new object (wooden cylinder) was placed in the cage at a location opposite to where the mouse was positioned. The mouse's behavior was video-recorded from above at 10 Hz. Three episodes of contact-sniffing behavior were analyzed for each mouse in conjunction with breathing cycles and fiber-photometry recording. The onset of sniffing was defined by the moment that the mouse contacted the object with its nostril, whereas the termination of sniffing was defined by the moment it retracted.

EPM

A custom-built plus-shaped maze made with white Plexiglass (77-cm long arms and 7-cm square-shaped center plate), 70 cm above the floor. For the EPM test, mice were tethered to electric and optical patch cords, placed on the center plate and allowed to voluntarily explore the environment for 10 min. Behavior was video-recorded from the top at 10 Hz using a custom-built LabView VI. For data synchronization, pyPhotometry and breathing monitoring (PowerLab) systems received a TTL signal (5 V) generated by a cDAQ NI-9401 device (National Instruments; operated by the LabView software). For photoinhibition experiments with

low baseline anxiety, mice were handled and habituated to optic-cord tethering for 5–10 min a day for 7 days. On the test day, mice were tethered to an optical patch cord and then placed in the center plate of the EPM arena. Mice were allowed to explore the environment for 15 min. Light was delivered during the second epoch (5–10 min of 15 min) of experiments.

Elevated platform

The elevated platform consisted of a circular plastic platform (12 cm diameter), 100 cm above the ground, on top of a tripod. An opaque plastic tube (15 cm in height and 11 cm in diameter) was placed on top of the platform. Mice were tethered to electric and optical patch cords and placed in the cylinder. After acclimation for 15 min, the tube was gently lifted by hand, and mice were exposed to an inescapable height. Behavior was video-recorded from the side at 10 Hz.

RTPP

A two-chambered white Plexiglass box ($W \times D \times H = 60 \times 30 \times 30 \text{ cm}$) was used for the RTPP test. Mice were tethered to optical patch cords, placed in the testing arena and allowed to freely explore the environment for 30 min. Behavior was video-recorded from the top at 10 Hz, and the location of the mouse (body center) was monitored in real time using EthoVision 11 tracking software (Noldus). During the second epoch (the second 10 min), one of the chambers was paired with photostimulation. The pairing of the stimulated chamber (left or right) was counterbalanced.

Female odor preference

Male mice were used for the female odor preference test. Mice were tethered to optical patch cords and placed in the same two-chamber testing arena. Bedding was collected from a female mouse cage housed for 4 days before the experiments^{51,52}. One side of the testing box (counterbalanced for each subject) was equipped with a 30 mm Petri dish that contained the bedding. Male mice were allowed to freely explore the environment for 30 min. During the second epoch (10 min), photostimulation was paired with the side of the chamber with the bedding.

Trimethylthiazoline (TMT) avoidance test

A plastic cage ($W \times D \times H = 47 \times 26 \times 21 \text{ cm}$) was used for the TMT avoidance test. One side of the cage (counterbalanced for each subject) was equipped with a 30 mm Petri dish that contained 300 μl of 10% TMT. Mice were allowed to freely explore the environment for 15 min. Photostimulation was delivered during the second epoch (5 min).

Light/dark choice test

A white Plexiglass arena ($W \times D \times H = 41 \times 41 \times 30 \text{ cm}$) was equipped with an opaque shade ($W \times D \times H = 40 \times 20 \times 20 \text{ cm}$). The apparatus was placed under illumination, and half the arena (dark zone) was covered by the shade. For photoinhibition experiments with low baseline anxiety, mice were handled and habituated to optic-cord tethering for 5–10 min a day for 7 days. A rotary joint (HRJ_OE_12_FC; Doric Lenses) with electric and optical connectors was used for electric and optical patch cords. On the test day, mice were tethered to patch cords, placed in the testing arena and then allowed to freely explore the environment for 10 min. Median breathing rate throughout the 10-min testing (in both light and dark zones) was calculated.

Electrophysiology

Mice were anesthetized with isoflurane and transcardially perfused with ice-cold cutting solution (230 mM sucrose, 2.5 mM KCl, 1 mM NaH₂PO₄, 21 mM NaHCO₃, 10 mM D-glucose, 1 mM CaCl₂ and 5 mM MgCl₂ (pH 7.3–7.35)). Mice were decapitated, and their brains were quickly removed and chilled in an ice-cold cutting solution. Coronal slices (300 μm) were cut with a vibratome (Leica 657 VT1200) and then incubated in a storage chamber containing artificial cerebrospinal fluid (126 mM

NaCl, 2.5 mM KCl, 1.2 mM NaH₂PO₄, 21.4 mM NaHCO₃, 10 mM D-glucose, 2.4 mM CaCl₂ and 1.2 mM MgCl₂ (pH 7.3–7.4) at 34 °C for at least 1 h. All solutions were continuously bubbled with 95% O₂/5% CO₂. Whole-cell patch-clamp recordings were obtained using an amplifier (Molecular Devices; 665 MultiClamp 700B) and filtered at 2 kHz. Patch electrodes (2–5 MΩ) were filled with a potassium gluconate internal solution (130 mM K-gluconate, 2 mM HEPES, 2 mM NaCl, 0.25 mM EGTA, 4 mM MgCl₂, 4 mM ATP and 0.4 mM GTP (pH 7.29)). CRACM experiments were conducted in voltage-clamp mode at a holding potential of −70 mV. Three light pulses (5 ms) were delivered 2.5 s apart, triggered through pClamp software (Molecular Devices). Only cells with access resistance <25 MΩ throughout the recording were used in the analysis.

Histology

Mice were transcardially perfused with PBS, followed by 4% paraformaldehyde dissolved in phosphate buffer (4% PFA/PB). Brains were fixed in 4% PFA/PB for 12–16 h, cryoprotected in 30% sucrose/PB for 48 h and then sectioned coronally (40 µm thickness) on a −20 °C cryostat (Leica CM1950). From each group of experiments using virus or tracer injections, maximal fluorescence intensity was calculated in a 0–255 digital brightness scale. Pixels that exceeded the 50% threshold of this value were included in the area of viral expression or CTB spread estimated in each animal, and these areas were overlaid to visualize the group average. Center points of the area that exceeded the 80% threshold were marked as the center of expression.

Immunohistochemistry

Brain sections covering AP −4.9 to −5.0 mm were collected from three mice (three sections from each, nine sections total). Sections were incubated in blocking solution (0.3% Triton X-100 and 2% normal donkey serum, dissolved in PBS) for 1 h at room temperature, rinsed with PBST three times and incubated with rabbit anti-GAD67 (Merck Millipore, SAB4300642; 1:1,000, dissolved in blocking solution) primary antibody for 16 h. The following day, the sections were rinsed with PBST and incubated with Cy3-conjugated donkey anti-rabbit IgG (Jackson ImmunoResearch, AB_2307443; 1:500, dissolved in blocking solution) secondary antibody for 2 h. After rinsing with PBS, sections were mounted on glass slides and coverslipped with DAPI Fluoromount-G solution (Thermo Fisher Scientific).

Microscopy

Images were taken with a BZ-X710 all-in-one fluorescence microscope (Keyence). Region-wide images to confirm construct (AAV) expression were taken at ×4 and ×10 magnification. Precise images for observing axon terminals were taken at ×20 magnification. Confocal microscopy images for colocalization analyses were taken using an FV3000 confocal laser scanning microscope (Olympus). Three to four images were taken from each brain section at ×40 magnification. Serial Z-stack images were taken (6–12 planes, 1.0 aerial unit). To quantify PnC^{GABA} projection terminals, fluorescence density was calculated by subtracting the background brightness (ventral striatum area where no terminals were observed) from projection areas in each mouse (Adobe Photoshop 2023).

Randomization and data inclusion

No statistical methods were used to predetermine sample sizes, and animals were randomly assigned to groups. Manual behavioral scoring was blinded. Breathing measurements were automatically performed by LabChart software. All mice that had viral expressions in the region of interest (at least one side in case of bilateral target experiments) were included in the data. Mice that had no viral expression due to a mistake in surgery were excluded from the data.

Statistical analyses

Statistical analyses were performed using GraphPad Prism 7. Normality was tested by the Shapiro–Wilk normality test ($n \geq 7$) or

Kolmogorov–Smirnov test ($n < 7$). In case the normality test failed ($P < 0.05$), nonparametric tests were performed. Two-tailed paired *t* test and Wilcoxon signed rank test were used for within-group analysis. Two-tailed unpaired *t* test and Mann–Whitney *U* test were used for between-group analysis. Repeated measures (RM) two-way analysis of variance followed by Sidak's post hoc test was used for between-group comparison with RMs. Details of statistical tests are described in Supplementary Table 1.

Reporting summary

Further information on research design is available in the Nature Portfolio Reporting Summary linked to this article.

Data availability

All data are available from the corresponding author upon request. All data associated with statistical analyses are available as source data. The source data are also available at figshare repository (<https://doi.org/10.6084/m9.figshare.26888749> (ref. 53)). Source data are provided with this paper.

References

51. Liu, Y. et al. Molecular regulation of sexual preference revealed by genetic studies of 5-HT in the brains of male mice. *Nature* **472**, 95–99 (2011).
52. Beny-Shefer, Y. et al. Nucleus accumbens dopamine signaling regulates sexual preference for females in male mice. *Cell Rep.* **21**, 3079–3088 (2017).
53. Jhang, J. et al. A top-down slow breathing circuit that alleviates negative affect. *figshare* <https://doi.org/10.6084/m9.figshare.26888749> (2024).

Acknowledgements

We thank all members of the Han Laboratory for scientific discussions and support. This work was supported by grants from the KAVLI Institute for Brain and Mind Innovative Research Grants (IRGS 2020-1710). All members of the Han Laboratory are committed to upholding principles of equity and inclusion, ensuring that no person is discriminated against based on gender, race, age, religion, sexual orientation, veteran status or disability.

Author contributions

S.H. and J.J. designed the study and secured funding. J.J., S.P., D.D.O. and S.H. wrote the paper. J.J. performed the experiments and analyzed the data. S.P. performed electrophysiology. S.L. helped with thermistor implantation surgeries.

Competing interests

The authors declare no competing interests.

Additional information

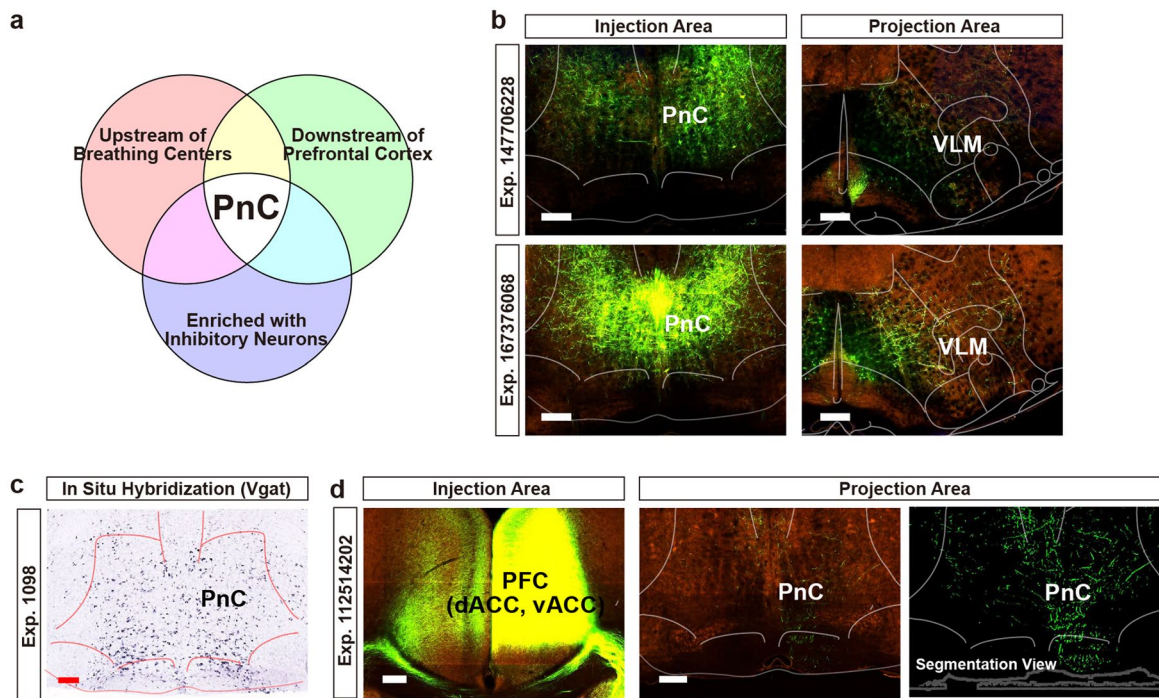
Extended data is available for this paper at <https://doi.org/10.1038/s41593-024-01799-w>.

Supplementary information The online version contains supplementary material available at <https://doi.org/10.1038/s41593-024-01799-w>.

Correspondence and requests for materials should be addressed to Sung Han.

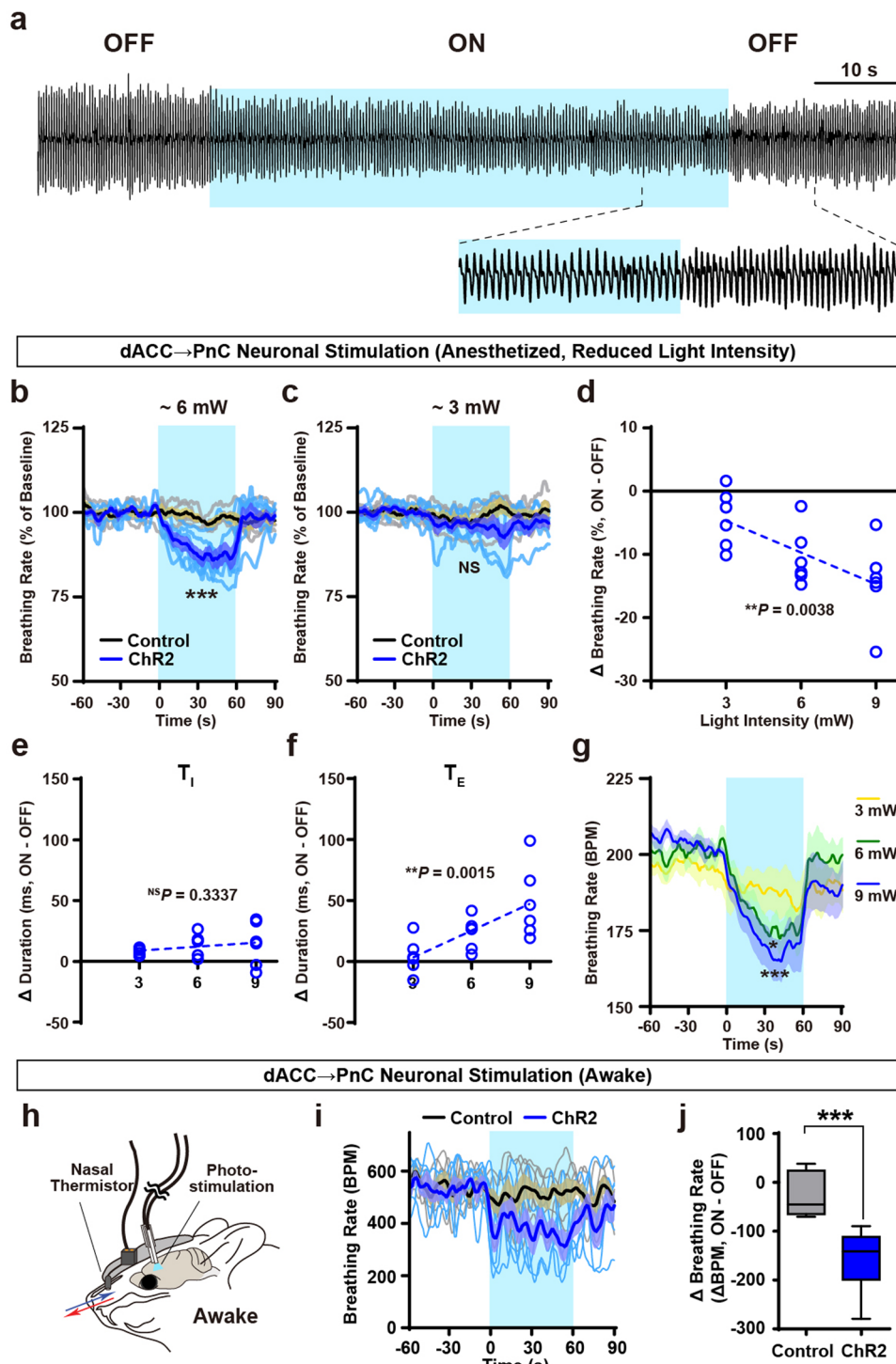
Peer review information *Nature Neuroscience* thanks Julien Bouvier, Nadine Gogolla and the other, anonymous, reviewer(s) for their contribution to the peer review of this work.

Reprints and permissions information is available at www.nature.com/reprints.



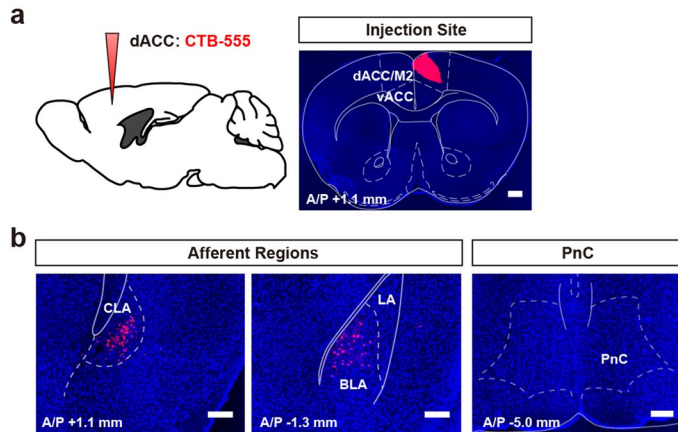
Extended Data Fig. 1 | Allen Brain Atlas-based search for potential top-down breathing circuits. **a**, Summary of the criteria used to search candidate circuits. Axonal projection images were searched through the Mouse Brain Connectivity Atlas (Allen Brain Institute). In situ hybridization (ISH) images were searched through the Mouse Brain ISH Data Atlas (Allen Brain Institute). **b**, Sample images showing the projections of labeled PnC neurons observed in the ventrolateral medulla (VLM). Left, the AAV injection site (PnC). Right, the observed terminals in

the VLM. **c**, Sample image from a *Vgat* ISH experiment. **d**, Sample images showing the projections of PFC neurons observed in the PnC. Left image shows the AAV injection site (PFC, prefrontal cortex; covering the dACC and vACC) with the expression of eGFP. Middle and right (in segmentation view) images show the eGFP-labeled axon terminals in the PnC. PnC, pontine reticular nucleus; VLM, ventrolateral medulla; PFC, prefrontal cortex. Scale bars, 200 μ m in **b–d**. These are representative data (**b–d**) available from the Allen Brain Atlas.



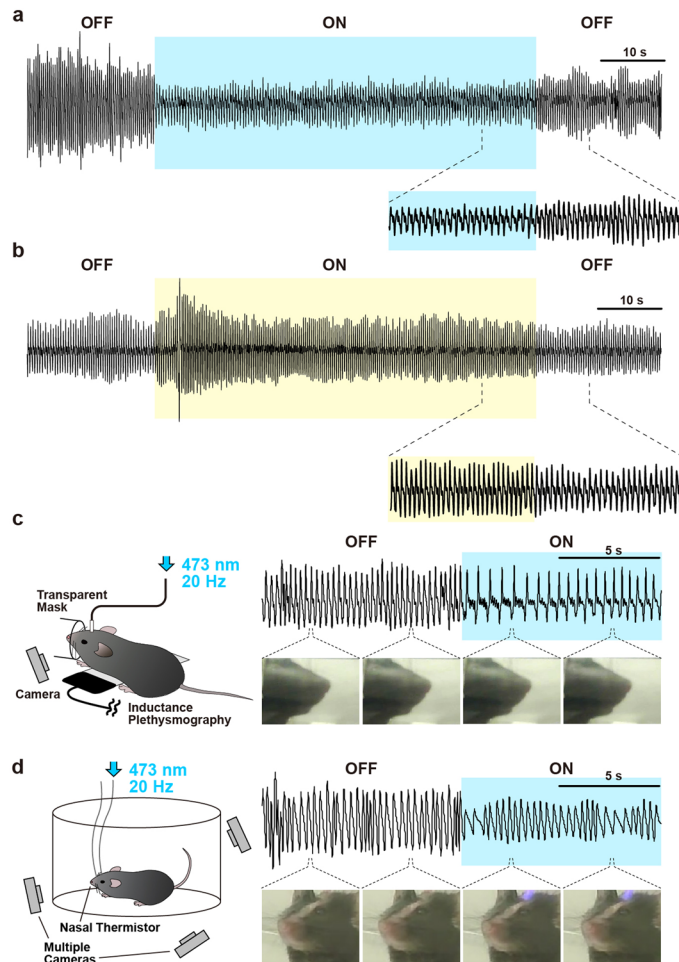
Extended Data Fig. 2 | Photoactivation of dACC → PnC neurons with breathing measurement. **a**, Representative raw breathing trace measured by inductance plethysmography experiment under anesthesia from a mouse expressing ChR2 in dACC → PnC neurons. **b–f**, Analyses of breathing rates and inspiratory/expiratory durations during photoactivation of dACC → PnC neurons with reduced light intensity (**b–f**; ChR2, N = 6; eGFP, N = 5 mice). **b,c**, Percent change of normalized breathing rates during the photoactivation with -6 mW (**b**) and -3 mW (**c**) intensity. **d**, Correlation between the change of breathing rate and intensity of light stimulation. **e,f**, Correlation between the change of

inspiratory (**e**) or expiratory (**f**) duration and intensity of light stimulation. **g**, Photoactivation of dACC → PnC neurons decreases breathing rates (shown in breath per minute; BPM). **h**, Schematic of breathing monitoring using a nasal thermistor sensor. **i,j**, Photoactivation of dACC → PnC neurons led to a decrease in breathing rate in awake mice (ChR2, N = 6; eGFP N = 6 mice). Average breathing rate (5-s window smoothed; **i**); light-induced changes (ON–OFF) in breathing rates (**j**). $^{\text{NS}}P > 0.05$, $^{\text{*}}P < 0.05$, $^{\text{**}}P < 0.01$, $^{\text{***}}P < 0.001$. Line graphs are shown as mean \pm s.e.m. Box-whisker plot is shown as median and interquartile range with minimum and maximum.



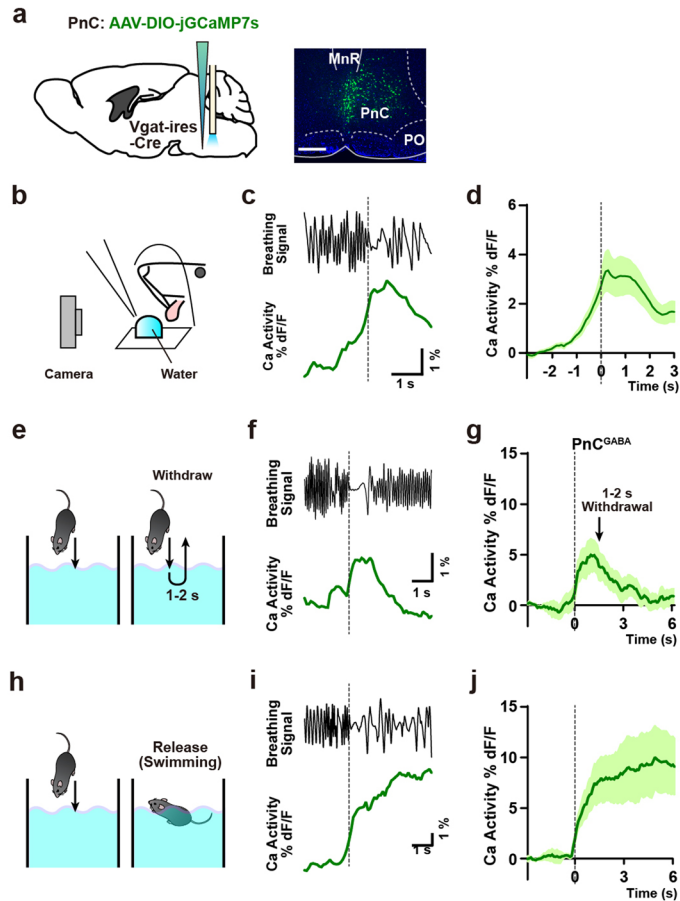
Extended Data Fig. 3 | Retrograde tracing from the dACC does not label neurons in the PnC. **a**, Schematic of CTB-555 injection into the dACC (left) and representative image showing the injection site (right). Scale bar, 500 μ m. **b**, Known afferent regions of the dACC (claustrum and basolateral amygdala) and

the PnC. No retrograde labeling occurred in the PnC ($N = 4$ mice). CLA, claustrum; LA, lateral nucleus of amygdala; BLA, basolateral nucleus of amygdala. Scale bar, 200 μ m.



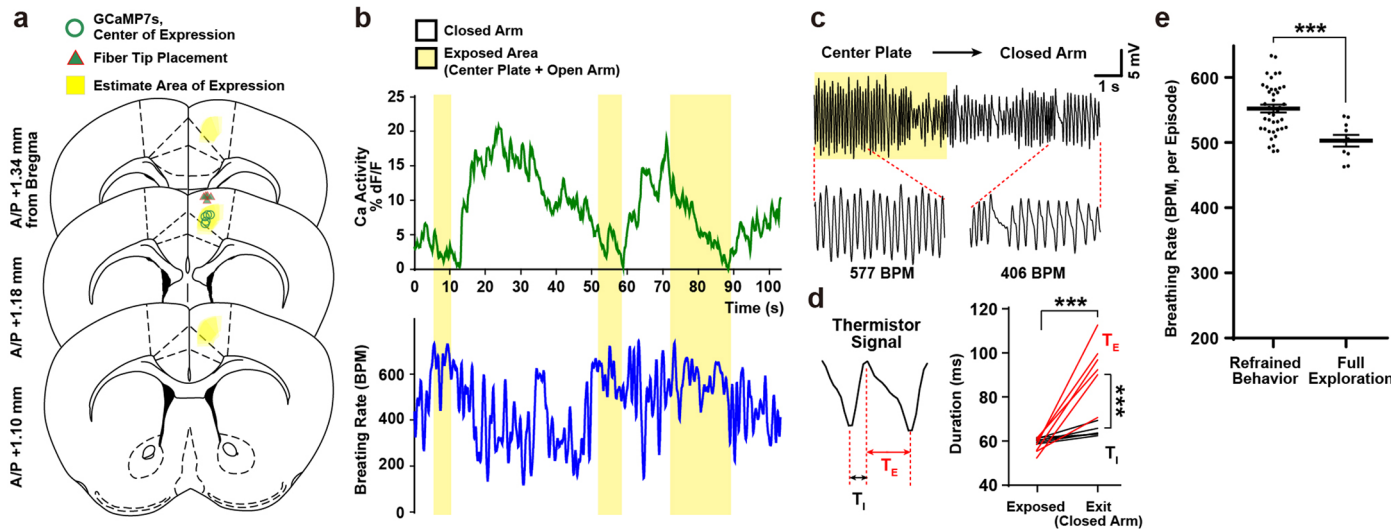
Extended Data Fig. 4 | Raw breathing traces and jaw movement recording during optogenetic stimulation of PnC^{GABA} neurons. **a**, Raw breathing trace recorded during ChR2-mediated photoactivation of PnC^{GABA} neurons. Scale bar, 10 s. **b**, Raw breathing trace recorded during eNpHR3.0-mediated photoinhibition of PnC^{GABA} neurons. Scale bar, 10 s. **c,d**, Schematic of

simultaneous recording of jaw movement and breathing signals using inductance plethysmography under anesthesia (**c**, left) or using nasal thermistor sensor in awake state (**d**, left). No instance of jaw opening or mastication was observed throughout the duration of photostimulation (right; **c**, N = 4 mice; **d**, N = 5 mice).



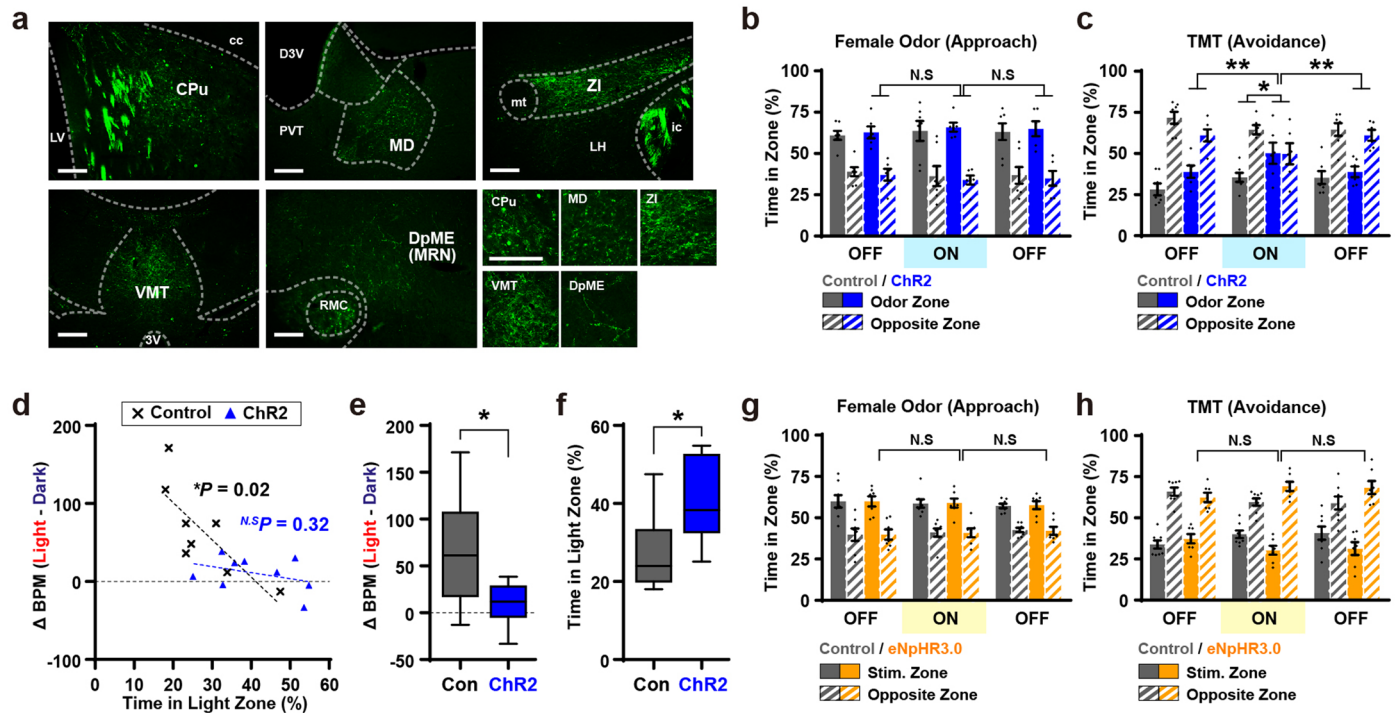
Extended Data Fig. 5 | Response of PnC^{GABA} neurons to drinking and swimming. **a**, Surgical procedure for expressing jGCaMP7s in PnC^{GABA} neurons, and image showing jGCaMP7s expression (right). Scale bar, 200 μm. **b**, Schematic showing observation of voluntary drinking behavior. **c**, Representative traces showing breathing cycles and PnC^{GABA} activity during drinking behavior. **d**, Average PnC^{GABA} activity during drinking behavior (N = 5 mice). Dashed line shows the moment that a water droplet was taken into oral cavity. **e**, Schematic of submersion experiments in which mice were removed after 1–2 s (withdrawal).

f, Representative traces showing breathing cycles and PnC^{GABA} activity during withdrawal experiments. **g**, Average PnC^{GABA} neuronal activity during withdrawal experiments (N = 5 mice). **h**, Schematic of submersion experiments in which mice were released. **i**, Representative traces showing breathing cycles and PnC^{GABA} activity during release/swim experiments. **j**, Average PnC^{GABA} neuronal activity during release/swim experiments (N = 5 mice). Data are shown as mean ± s.e.m. or individual value from each subject.



Extended Data Fig. 6 | Extended data related to breathing and dACC→PnC activity measurements during EPM exposure. **a**, Illustrations showing GCaMP7s injection sites and fiber placement targeting dACC area, in mice used for elevated plus maze, elevated platform and foot shock exposure experiments (N = 6 mice). **b**, Representative traces of dACC→PnC neuronal activity (top) and breathing rate (bottom) during the elevated plus maze exposure.

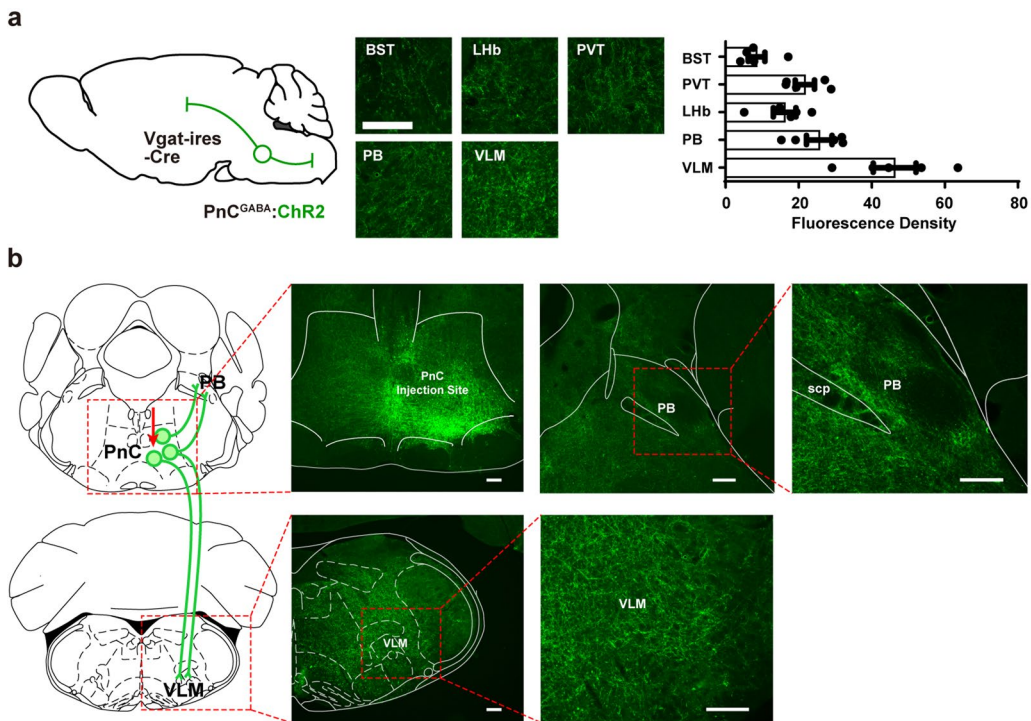
c, Representative raw breathing signals observed during an exit episode. **d**, Analysis of the length of inspiratory and expiratory phases before and after exit (N = 6 mice). **e**, Breathing rates during exploration of an exposed area classified by episodes with refrained behavior (n = 43 episodes) and full exploration (n = 10 episodes). ***P < 0.001. Data are shown as mean ± s.e.m. or individual value from each subject.



Extended Data Fig. 7 | Axon collaterals of dACC→PnC neurons and behavioral tests with photoactivation or photoinhibition of the dACC→PnC pathway.

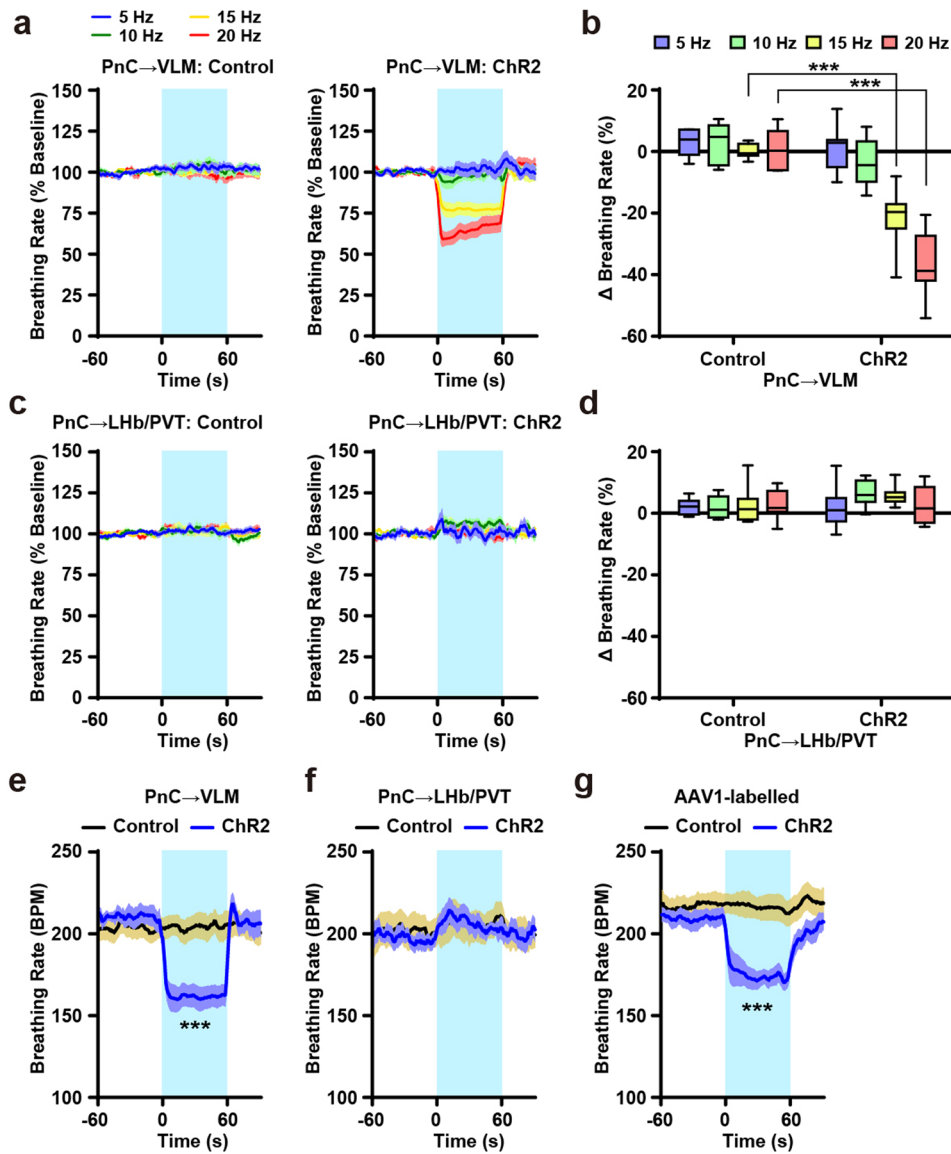
a, Axon collaterals of dACC→PnC neurons observed in regions other than the PnC. Scale bar, 200 μ m. **b,c**, Photoactivation of dACC→PnC neurons (ChR2, N = 6; eGFP, N = 7 male mice) did not change approach response to female odor (**b**) but reduced avoidance response to TMT (**c**). **d–f**, Photoactivation of dACC→PnC neurons during light/dark choice test (**d**, ChR2, N = 9 and eGFP control, N = 8 mice). Photoactivation of dACC→PnC neurons reduces Δ BPM (light–dark; **e**) and increases time spent in the light zone (**f**). **g,h**, Photoinhibition of dACC→PnC

projections (eNpHR3.0, N = 7; eGFP control, N = 8 male mice) did not change approach response to female odor (**g**) or avoidance response to TMT (**h**). LV, lateral ventricle; CPu, caudate putamen; cc, corpus callosum; D3V, dorsal third ventricle; PVT, paraventricular thalamic nucleus; MD, mediodorsal thalamic nucleus; VMT, ventromedial thalamic nucleus; DpME, deep mesencephalic nucleus; RMC, red nucleus, magnocellular; ZI, zona incerta; LH, lateral hypothalamus; mt, mammillothalamic tract; ic, internal capsule. $^{**}P < 0.01$, $^{*}P < 0.05$, $^{NS}P > 0.05$. Bar graphs are shown as mean \pm s.e.m. Box-whisker plots are shown as median and interquartile range with minimum and maximum.



Extended Data Fig. 8 | Efferent projections of PnC^{GABA} neurons. a, Efferent projections of PnC^{GABA} neurons. Right, quantification of projection density of eYFP-labeled axons (N = 5 mice, *Vgat-ires-Cre*). Scale bar, 200 μm. **b,** Images showing the viral injection site in the PnC, and brainstem regions receiving

efferent fibers expressing ChR2-eYFP. Scale bar, 200 μm. BST, bed nucleus of stria terminalis; Lhb, lateral habenula; PVT, paraventricular nucleus of thalamus; PB, parabrachial nucleus; VLM, ventrolateral medulla. Data are shown as mean ± s.e.m.



Extended Data Fig. 9 | Measurement of breathing rate during photoactivation of PnC^{GABA} terminals. **a**, Inductance plethysmography experiments performed with photoactivation of PnC^{GABA}→VLM terminals (ChR2, N = 7; eGFP, N = 7 mice), tested with different frequencies. **b**, Changes in breathing rates (% of baseline) induced by stimulation of PnC^{GABA}→VLM terminals (ChR2, N = 7; eGFP, N = 7 mice). **c**, Inductance plethysmography experiments performed with photoactivation of PnC^{GABA}→LHb/PVT terminals (ChR2, N = 7; eGFP, N = 8 mice), tested with different frequencies. **d**, Changes in breathing rates (% of baseline) induced by stimulation of PnC^{GABA}→LHb/PVT terminals (ChR2, N = 7; eGFP, N = 8 mice). **e–g**, Breathing rates shown as breaths per minute (BPM) during photoactivation experiments (15-Hz stimulation; **e**, PnC^{GABA}→VLM; **f**, PnC^{GABA}→LHb/PVT; **g**, AAV1-based labeling). ***P < 0.001. Line graphs are shown as mean ± s.e.m. Box-whisker plots are shown as median and interquartile range with minimum and maximum.

eGFP, N = 8 mice), tested with different frequencies. **d**, Changes in breathing rates (% of baseline) induced by stimulation of PnC^{GABA}→LHb/PVT terminals (ChR2, N = 7; eGFP, N = 8 mice). **e–g**, Breathing rates shown as breaths per minute (BPM) during photoactivation experiments (15-Hz stimulation; **e**, PnC^{GABA}→VLM; **f**, PnC^{GABA}→LHb/PVT; **g**, AAV1-based labeling). ***P < 0.001. Line graphs are shown as mean ± s.e.m. Box-whisker plots are shown as median and interquartile range with minimum and maximum.

Reporting Summary

Nature Portfolio wishes to improve the reproducibility of the work that we publish. This form provides structure for consistency and transparency in reporting. For further information on Nature Portfolio policies, see our [Editorial Policies](#) and the [Editorial Policy Checklist](#).

Statistics

For all statistical analyses, confirm that the following items are present in the figure legend, table legend, main text, or Methods section.

n/a Confirmed

- The exact sample size (n) for each experimental group/condition, given as a discrete number and unit of measurement
- A statement on whether measurements were taken from distinct samples or whether the same sample was measured repeatedly
- The statistical test(s) used AND whether they are one- or two-sided
Only common tests should be described solely by name; describe more complex techniques in the Methods section.
- A description of all covariates tested
- A description of any assumptions or corrections, such as tests of normality and adjustment for multiple comparisons
- A full description of the statistical parameters including central tendency (e.g. means) or other basic estimates (e.g. regression coefficient) AND variation (e.g. standard deviation) or associated estimates of uncertainty (e.g. confidence intervals)
- For null hypothesis testing, the test statistic (e.g. F , t , r) with confidence intervals, effect sizes, degrees of freedom and P value noted
Give P values as exact values whenever suitable.
- For Bayesian analysis, information on the choice of priors and Markov chain Monte Carlo settings
- For hierarchical and complex designs, identification of the appropriate level for tests and full reporting of outcomes
- Estimates of effect sizes (e.g. Cohen's d , Pearson's r), indicating how they were calculated

Our web collection on [statistics for biologists](#) contains articles on many of the points above.

Software and code

Policy information about [availability of computer code](#)

Data collection

LabChart Pro 8 was used for collection of breathing data. Open source code from pyPhotometry in Python 3.7 was used for GCaMP signal (neuronal activity) data collection. LabView 2018 was used for camera control and generation of synchronization signals.

Data analysis

LabChart Pro 8 was used for analyzing breathing data. Ethovision XT 11 was used for analyzing behavioral data with animal tracking. GraphPad Prism 7 was used for statistical analyses. Brightness scale analysis was performed using Adobe Photoshop 2024.

For manuscripts utilizing custom algorithms or software that are central to the research but not yet described in published literature, software must be made available to editors and reviewers. We strongly encourage code deposition in a community repository (e.g. GitHub). See the Nature Portfolio [guidelines for submitting code & software](#) for further information.

Data

Policy information about [availability of data](#)

All manuscripts must include a [data availability statement](#). This statement should provide the following information, where applicable:

- Accession codes, unique identifiers, or web links for publicly available datasets
- A description of any restrictions on data availability
- For clinical datasets or third party data, please ensure that the statement adheres to our [policy](#)

All statistical Source Data are accessible at Figshare repository (DOI:10.6084/m9.figshare.26888749). All data are available from the corresponding author upon reasonable request. Microscopic image data in Extended Data Fig.1 are available from the Allen Brain atlas.

Human research participants

Policy information about [studies involving human research participants and Sex and Gender in Research](#).

Reporting on sex and gender

N/A

Population characteristics

N/A

Recruitment

N/A

Ethics oversight

N/A

Note that full information on the approval of the study protocol must also be provided in the manuscript.

Field-specific reporting

Please select the one below that is the best fit for your research. If you are not sure, read the appropriate sections before making your selection.

Life sciences

Behavioural & social sciences

Ecological, evolutionary & environmental sciences

For a reference copy of the document with all sections, see nature.com/documents/nr-reporting-summary-flat.pdf

Life sciences study design

All studies must disclose on these points even when the disclosure is negative.

Sample size

Adequate sample size was confirmed by power analysis. All behavioral data used more than or equal to 6 animals per group (n = 6-11).

Data exclusions

Two mice with no viral expression were excluded from the anesthetized plethysmography experiment with optogenetics (ChR2).

Replication

Detailed methods, surgical procedures, and resources were described in the Method section to ensure data replication. Expression of viral constructs were confirmed by histological analysis after behavioral experiments. All retrograde and anterograde tracing experiments were successful. All optogenetic experiments with respiratory and behavioral measurements were successfully replicated, except for the cases with no viral expression.

Randomization

All subjects were randomly assigned to groups.

Blinding

Behavioral data were manually scored by blinded investigators using randomized video files after acquisition. Respiratory measurements were analyzed automatically by LabChart Pro 8 software, so blinding was not necessary. Histological analyses (including CTB or viral tracer injections and projection density measurements) were conducted within single groups without comparison, making blinding unnecessary.

Reporting for specific materials, systems and methods

We require information from authors about some types of materials, experimental systems and methods used in many studies. Here, indicate whether each material, system or method listed is relevant to your study. If you are not sure if a list item applies to your research, read the appropriate section before selecting a response.

Materials & experimental systems

n/a	Involved in the study
<input type="checkbox"/>	<input checked="" type="checkbox"/> Antibodies
<input checked="" type="checkbox"/>	<input type="checkbox"/> Eukaryotic cell lines
<input checked="" type="checkbox"/>	<input type="checkbox"/> Palaeontology and archaeology
<input type="checkbox"/>	<input checked="" type="checkbox"/> Animals and other organisms
<input checked="" type="checkbox"/>	<input type="checkbox"/> Clinical data
<input checked="" type="checkbox"/>	<input type="checkbox"/> Dual use research of concern

Methods

n/a	Involved in the study
<input checked="" type="checkbox"/>	<input type="checkbox"/> ChIP-seq
<input checked="" type="checkbox"/>	<input type="checkbox"/> Flow cytometry
<input checked="" type="checkbox"/>	<input type="checkbox"/> MRI-based neuroimaging

Antibodies

Antibodies used

rabbit anti-GAD67 (1:1000; Merck Millipore SAB4300642)
Cy3-conjugated AffiniPure donkey anti-rabbit IgG (1:500; Jackson Immunoresearch Labs, AB_2307443)

Validation

The specificity of primary antibody was validated by the manufacturer (Western blot data, Merck Millipore), and supported by Speigel et al. (2019).

Animals and other research organisms

Policy information about [studies involving animals](#); [ARRIVE guidelines](#) recommended for reporting animal research, and [Sex and Gender in Research](#)

Laboratory animals

Adult (2-4 months old) mice were used from both sexes in all experiments. C57Bl/6J (#000664) and Vgat-ires-Cre (#028862) mouse lines were obtained from the Jackson laboratory.

Wild animals

This study did not involve wild animals.

Reporting on sex

Both male and female mice were used in all experiments, except male-specific behavioral tests (preference test for female cage odor). Male and female mice were randomly assigned to groups.

Field-collected samples

This study did not involve samples collected from the field.

Ethics oversight

All protocols for animal experiments were approved by institutional animal care and use committee (IACUC) of the Salk Institute for Biological studies in accordance with the NIH guidelines for animal experimentation.

Note that full information on the approval of the study protocol must also be provided in the manuscript.